Simulation of bridging mechanisms in complex laminates using a hybrid PF-CZM method

A.R. Dusane[a,d], P.R. Budarapu[a,*], A.K. Pradhan[a], S. Natarajan[b], J. Reinoso[c], M. Paggi[d]

[a]*School of Mechanical Sciences, Indian Institute of Technology, Bhubaneswar 752050, India.*
[b]*Department of Mechanical Engineering, Indian Institute of Technology Madras, Chennai 600036.*
[c]*Elasticity and Strength of Materials Group, School of Engineering, Universidad de Sevilla, Camino de los Descubrimientos s/n, 41092, Seville, Spain.*
[d]*IMT School for Advanced Studies Lucca, 19 Piazza San Francesco, 55100 Lucca, Italy.*

Abstract

Delamination and cracking of matrix/fiber is a common failure phenomena reported in fiber reinforced composite. As complex stress states develop in laminated structures, they are prone to fractures. Therefore, designs with large damage tolerance are currently implemented in most of the industrial sectors. This can be achieved by designing the composites for failure, which requires a comprehensive understanding of failure mechanisms. Cohesive Zone Models (CZM) are a popular technique to study debonding and decohesion in composite structures. Furthermore, due to the accurate simulation of complex crack paths including crack branching, the Phase Field (PF) approach has gained notable relevance in fracture studies, including the interplay between laminae-laminate debonding and crack propagation in the matrix. Bridging mechanisms in intralayer and interlayer and crack simulation coupling the phase field approach and the cohesive zone model is herein used for identifying crack migration through material layers. The crack paths and the related force-displacement curves of 2D multi-layered material models of complex laminates are predicted and compared.

Keywords: Complex laminates; Bridging mechanisms; Delamination-migration; Cohesive Zone Model; Phase-field model.

1. Introduction

Composites are engineered materials made of two or more constituents having different physical and/or chemical properties. The constituent materials are combined to achieve the material properties that are better than those of the individual parent materials [1, 2, 3]. Common composites include: metal-matrix composites, ceramic matrix composites, fiber reinforced composites [4], multifunctional composites [5], to name a few. The main focus of this study is to understand the failure mechanisms of laminated composites, made by embedding laminae layers of different stiffness in the matrix.

The properties of the fiber reinforced composites mainly depend on the fiber-orientation [6]. Fiber cracking, matrix failure, and interface debonding/delamination are prominent failure mechanisms in laminated composites [7]. Fiber cracking results in the degradation of strength and stiffness of the composite, whereas matrix cracking results in the collapse of the entire component [7, 8]. Delamination starts at edges and might arise due to manufacturing defects. The occurence of this phenomenon prevents the load transfer between the matrix and the fiber [9, 8]. Among the aforementioned failure mechanisms, the formation and subsequent propagation of matrix-macro cracks followed by interface failure is the dominant mode of failure in fiber-reinforced composites. The crack propagation through different materials and crack growth are associated with different energy release mechanisms, as shown in Fig. 1. Furthermore, strength and fracture toughness of the composite depends on the nature of interface and crack orientation impinging onto the interface [10, 11].

The fracture behavior of multilayer Silicon Nitride/Boron Nitride Ceramics has been studied in [12], where the authors reported crack deflection along weak interface is considered to be the major factor for improving fracture toughness. Weak interfaces makes the crack path tortuous, thus increasing the total energy dissipation at failure. This mechanism has been firstly theorized within the framework of linear elastic fracture mechanics (LEFM) by the so called Cooká Gordon mechanism [13], which is the result of crack branching and crack deflection with typical competition between crack penetration in the layers and delamination along with the existing interfaces. A theoretical framework to study the mechanics of stress transfer through both homogeneous and inhomogeneous interphases in a curved-fiber pull-out test and an analysis of the stress field in the three-phase composite system is developed in [14]. The effect of strong interfaces in alumina-aluminium titanate is

*Corresponding author. Tel: +91-674-713-7124
Email address: pattabhi@iitbbs.ac.in (P.R. Budarapu)

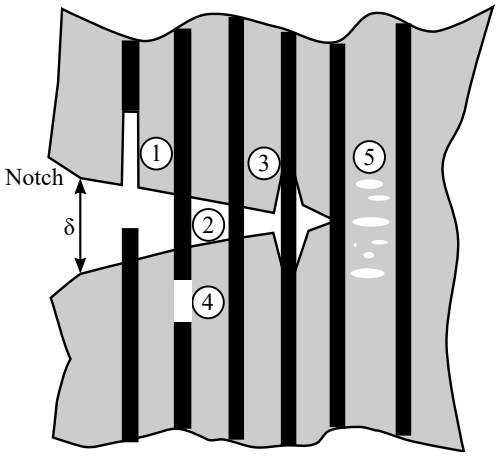

Figure 1: Typical damage modes in fiber reinforced composites.

studied in [15]. The presence of tough interfaces in composites leads to crack deflection. For whisker-reinforced metal matrix composites, failure due to debonding of the fiber-matrix interface has been analyzed in [16]. In [17], the role of elastic mismatch and the stress singularity of the crack at the interface between two bonded linear elastic materials was studied. Differing from the previous investigation, an analytical approach has been employed in [18], in order to study the mechanisms of crack penetration and delamination in composites. It was concluded that the crack penetration and deflection depends on the ratio of the toughness of the interface with respect to that of the bulk, with higher probability for asymmetric single-sided deflection. Cohesive zone models were employed in order to study the effect of modulus mismatch on the crack deflection at the interface. The framework of non-linear fracture mechanics using cohesive zone models has been provided in [19]. They noted that the effect of modulus mismatch on crack deflection is susceptible to the mixed-mode failure criterion for the interface, mainly if the cracked layer is much stiffer than the substrate.

In the recent years, the development of computational methods to predict crack initiation and propagation in engineering components has been a topic of intense research. The computational methods can be broadly classified as (a) discrete and (b) smeared/diffused approaches. In the discrete approach, the crack is represented as a sharp discontinuity either implicitly or explicitly. An explicit representation requires a conforming background discretization which possibly increase the computational cost when multiple cracks are involved or if crack propagation is required to be simulated. The crack can be represented implicitly using the partition of unity methods (PUM), element enrichment formulations like extended finite element method (XFEM), to name a few. Alternatively, cracks are diffused over certain region in diffused models.

The phase field method (PFM) is a diffused crack model based on the seminal works of Francfort and Marigo [20] and Miehe et al [21]. Within this framework, the entire fracture fracture processes (crack initiation, propagation and branching) are governed by minimization of energy functional. Phase field has been applied to variety of problems, for example: dynamic brittle fracture [20], fracture in biological tissues [22], thermal fracture [23], fracture of plates and shells [21]. PFM successfully applied to composite failure [24] and recently PFM coupled with cohesive elements has been proposed to model composite failure in [25, 26, 27, 6]. A numerical investigation of the applicability of an original bulk-interface fracture simulation technique to trigger branching, coalescence, shielding, and amplification of rock fracture in geo-materials within the context of the phase field approach for fracture is proposed in [28]. Recently, [29] studied crack propagation in variable stiffness composite laminates, although the effect of interface properties on crack propagation was not examined. A phase field model considering the interfacial damage for different configurations of a fiber reinforced composite is proposed in [30].

The main objective of the present study is to investigate the crack growth by modelling the interaction between crack penetration and cohesive delamination at interfaces with different elastic and fracture properties. To this end, a hybrid strategy by combining the phase field approach to simulate brittle fracture and the cohesive zone model to model the interface failure is proposed. We name the developed methodology as the 'hybrid PF-CZM' method and denote the constituents of the laminate, namely: matrix as 'constituent1' and that of the laminae as 'constituent2'.

The rest of the paper is organized as follows: Section 2 presents a brief overview of the phase field method and the cohesive zone model, along with the implementation aspects in finite element analysis program (FEAP). Numerical examples presented in Section 3, helpsto understand the influence of interphase on the crack growth in terms of crack penetration/debonding along the interface. Key results are summarized in Section 4.

2. Theoretical formulation

The current modeling formulation is developed in the general Euclidean space of dimension n_{dim} under infinitesimal deformation setting. Consider an arbitrary body occupying volume $\Omega \in \mathbb{R}^{n_{\mathrm{dim}}}$, where the boundaries of the body accommodate the following decomposition: $\partial\Omega \in \mathbb{R}^{n_{\mathrm{dim}}-1}$, as shown in Fig. 2. The kinematic and traction boundary conditions on disjointed parts of boundaries are: $\delta\Omega_{\mathrm{u}}$ and $\delta\Omega_{\mathrm{t}}$ satisfying $\delta\Omega_{\mathrm{u}} \cup \delta\Omega_{\mathrm{t}} = \delta\Omega$ and $\delta\Omega_{\mathrm{u}} \cap \delta\Omega_{\mathrm{t}} = 0$, then, the displacements and tractions on the boundaries are given by:

$$\mathbf{u} = \bar{\mathbf{u}} \quad \text{on} \quad \partial\Omega_u, \tag{1}$$

$$\bar{\mathbf{t}} = \boldsymbol{\sigma} \cdot \mathbf{n} \quad \text{on} \quad \partial\Omega_t \tag{2}$$

where n is the outward normal, and $\boldsymbol{\sigma}$ is the Cauchy stress tensor. The body forces are denoted by the vector, $\mathbf{f}_v : \Omega \rightarrow \mathbb{R}^{n_{\mathrm{dim}}}$. The composite is characterized by quasi-brittle interfaces, Γ_{i}, and a crack in the layer represented as an internal discontinuity, Γ_{b}. An arbitrary point in bulk can be represented by $\mathbf{x}$ while point on interface can be given by $\mathbf{x}_{\mathrm{c}}$ vectors in Cartesian co-ordinates. The free energy functional of body Ω is given

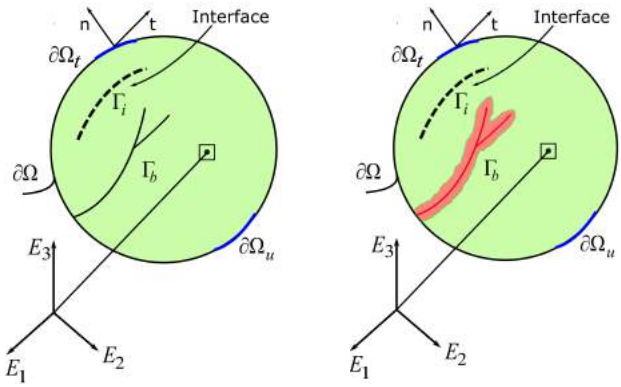

Figure 2: Schematic representation of (a) a sharp and (b) a smeared crack using the present coupled cohesive-phase field approach.

by [31]:

$$\Pi(\mathrm{u}, \Gamma) = \Pi_{\Omega}(\mathrm{u}, \Gamma) + \Pi_{\Gamma}(\Gamma) = \int_{\Omega \backslash \Gamma} \psi^{e}(\boldsymbol{\varepsilon}) \mathrm{d}\Omega + \int_{\Gamma} \mathcal{G}_c \mathrm{d}\Gamma \tag{3}$$

where, $\psi^{\mathrm{e}}(\boldsymbol{\varepsilon})$ is an elastic energy density, $\boldsymbol{\varepsilon}$ is strain field and $\mathcal{G}_c$ is fracture energy.

The above formulation is extended to couple the phase-field approach for brittle fracture, and the cohesive zone model by splitting the fracture energy function $\mathcal{G}_c$ into two parts:

$$\mathcal{G}_c = \mathcal{G}_c^b + \mathcal{G}_c^i, \tag{4}$$

where $\mathcal{G}_c^b$ denotes the fracture energy of the layers modeled by the phase-field approach and $\mathcal{G}_c^i$ represents the cohesive fracture energy of the interfaces modeled by the cohesive zone approach. Therefore, after substituting Eq. (4) into Eq. (3):

$$\Pi(\mathrm{u}, \Gamma_b, \Gamma_i) = \Pi_{\Omega} + \Pi_{\Gamma_b} + \Pi_{\Gamma_i} = \int_{\Omega \backslash \Gamma} \psi^{e}(\boldsymbol{\varepsilon}) \mathrm{d}\Omega + \int_{\Gamma_b} \mathcal{G}_c^b(\mathrm{u}, \mathfrak{d}) \mathrm{d}\Gamma + \int_{\Gamma_i} \mathcal{G}^i\left(\mathbf{g}, \mathfrak{h}, \mathfrak{d}\right) \mathrm{d}\Gamma \tag{5}$$

where, $\mathbf{g}$ denotes the vector of displacement discontinuities at the interface, $\mathfrak{h}$ is the history parameter which avoids re-healing of material and ensures uniqueness of solution [32] and $\mathfrak{d}$ is phase field degradation variable.

2.1. Phase field model for brittle fracture

In line with precedent developments, Miehe [31] and Bourdin et al.[33] have considered a smeared damage instead of sharp discontinuity, see Fig. 2. Within this framework the potential energy of bulk is expressed as:

$$\Pi_b(\mathrm{u}, \mathfrak{d}) = \int_{\Omega} \psi(\boldsymbol{\varepsilon}, \mathfrak{d}) \mathrm{d}\Omega + \int_{\Omega} \mathcal{G}_c^b \gamma(\mathfrak{d}, \nabla_{\mathrm{x}} \mathfrak{d}) \mathrm{d}\Omega, \tag{6}$$

where, $\psi(\boldsymbol{\varepsilon}, \mathfrak{d})$ is the elastic energy stored in the bulk, $\nabla_{\mathrm{x}}\bullet$ is the partial gradient operator, $\gamma(\mathfrak{d}, \nabla_{\mathrm{x}}\mathfrak{d})$ is known as the crack density functional [31], given by:

$$\gamma(\mathfrak{d}, \nabla_{\mathrm{x}}\mathfrak{d}) = \frac{1}{2l}\mathfrak{d}^2 + \frac{l}{2}|\nabla_{\mathrm{x}}\mathfrak{d}|^2 \tag{7}$$

where, l is phasefield internal length parameter which governs the sharpness of the crack, see Fig. 2(a). Furthermore, the elastic energy in Eq. (6) is expressed as:

$$\psi(\boldsymbol{\varepsilon}, \mathfrak{d}) = \mathfrak{g}(\mathfrak{d})\psi^e_+(\boldsymbol{\varepsilon}) + \psi^e_-(\boldsymbol{\varepsilon}), \tag{8}$$

where the elastic energy is split into positive and negative parts. The positive part of the elastic energy corresponds to the tensile stresses while the negative counterpart represents compressive stresses. Positive and negative stresses can be computed by differentiating the elastic energy with respect to the strain tensor, as shown below:

$$\psi^e_+(\boldsymbol{\varepsilon}) = \frac{\lambda}{2}\left(\langle \mathrm{tr}[\boldsymbol{\varepsilon}]\rangle_+\right)^2 + \mu \mathrm{tr}[\boldsymbol{\varepsilon}^2_+] \tag{9a}$$

and

$$\psi^e_-(\boldsymbol{\varepsilon}) = \frac{\lambda}{2}\left(\langle \mathrm{tr}[\boldsymbol{\varepsilon}]\rangle_-\right)^2 + \mu \mathrm{tr}[\boldsymbol{\varepsilon}^2_-], \tag{9b}$$

where λ and μ are the Lamé constants, tr denotes the trace operator, ε_+ and ε_- indicate the positive and the negative counterparts of the strain tensor, respectively, and the degradation function $\mathfrak{g}(\mathfrak{d})$ is expressed as:

$$\mathfrak{g}(\mathfrak{d}) = (1-\mathfrak{d})^2 + \mathcal{K}. \tag{10}$$

The introduction of positive and negative parts of the strain tensor leads to:

$$\sigma := \frac{\partial \psi}{\partial \varepsilon} = \mathfrak{g}(\mathfrak{d})\sigma_+ + \sigma_- \tag{11}$$

where

$$\sigma_\pm = \lambda\left(\langle \mathrm{tr}[\varepsilon]\rangle_\pm\right)1 + 2\mu\varepsilon_\pm. \tag{12}$$

Since the degradation function in Eq. (10) affects only the positive part, damage can develop only when the material is loaded under tension. Thus, no damage occurs when material loaded in compression.

2.2. Cohesive zone model compatible with phase-field

In this section, the linear cohesive zone model with tension cut-off [34] is considered to take into account the effect of the bulk damage $\mathfrak{d}$. The cohesive counterpart of the fracture energy in Eq. (5) is decomposed as the sum of Mode I and Mode II fracture energies, indicated by $\mathcal{G}_{\mathrm{I}}$ and $\mathcal{G}_{\mathrm{II}}$, respectively. The critical crack opening displacement, $\mathfrak{g}_{\mathrm{c}}$ relates to damage parameter linearly [26], i.e., $g_c(\mathfrak{d}) = (1-\mathfrak{d})g_{c,0} + \mathfrak{d}g_{c,1}$, where $g_{c,0} = g_c(\mathfrak{d}=0)$ and $g_{c,1} = g_c(\mathfrak{d}=1)$. The cohesive traction vs. relative displacement laws for Mode I and Mode II adopted in this study are given by, see Fig. 3:

$$\sigma = \begin{cases} k_n \frac{g_n}{g_{nc}}, & \text{if } 0 < \frac{g_n}{g_{nc}} < 1; \\ 0, & \text{if } \frac{g_n}{g_{nc}} \geq 1, \end{cases} \tag{13a}$$

$$\tau = \begin{cases} k_t \frac{g_t}{g_{tc}}, & \text{if } 0 < \frac{g_t}{g_{tc}} < 1; \\ 0, & \text{if } \frac{g_t}{g_{tc}} \geq 1. \end{cases} \tag{13b}$$

where σ and τ are the Mode I and Mode II tractions, respectively, g is the relative displacement, and the subscript n and t refers to opening and sliding modes, respectively. The stiffness in the cohesive relation, k, depends on damage variable $\mathfrak{d}$:

$$k_n = k_{n,0}\left(\frac{g_{nc,0}}{g_{nc}}\right)^2 \quad \text{and} \quad k_t = k_{t,0}\left(\frac{g_{tc,0}}{g_{tc}}\right)^2 \tag{14}$$

where k_0 and g_0 are the stiffness and critical relative displacements at $\mathfrak{d} = 0$, respectively.

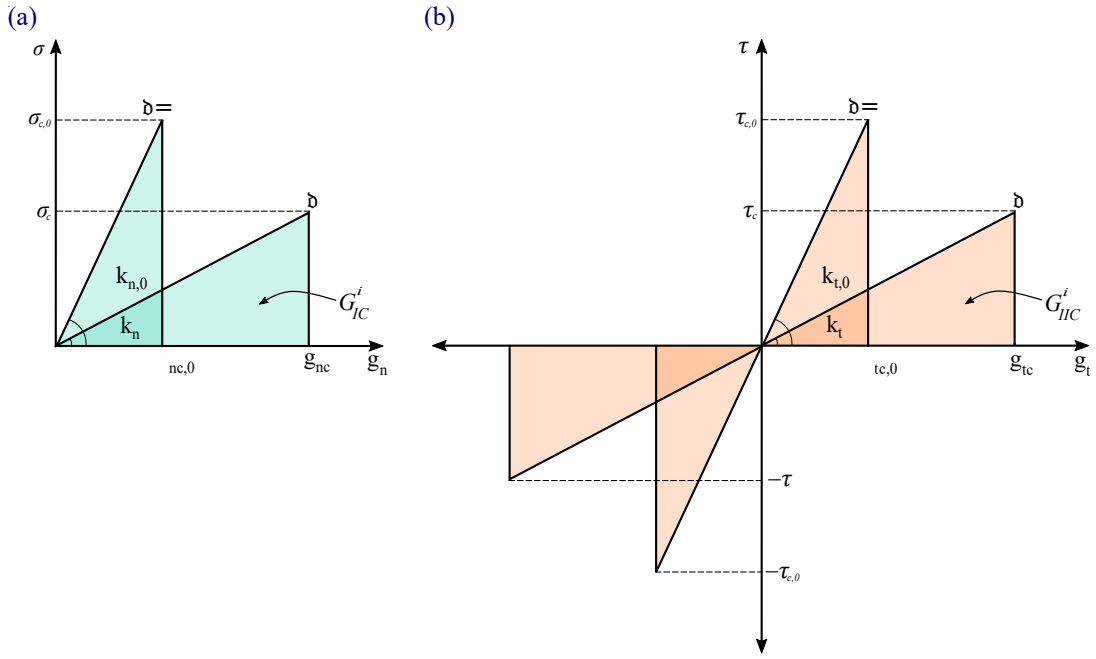

Figure 3: Schematic representation of the cohesive zone model coupled with the phase field variable for brittle fracture in the bulk. (a) Mode-I CZM traction σ vs g_{n} (b) Mode-II CZM traction τ vs g_{t} [25].

In this study, the critical energy release rate of the interface ($\mathcal{G}_c^i$) is assumed to be constant. This is because the model is formulated considering the Griffith energy criterion, followed by an explicit split of the total energy into the dissipated energy in the bulk fracture and the interface delamination in Eq. (4). As a result, $\mathcal{G}_c^i$ becomes the material parameter governing the interface failure, indicating the importance of interface fracture energy. The parameters in the interface energy ($\mathcal{G}_c^i$) and part of cohesive law are estimated from experiments.

The mixed-mode failure criterion enabling the interface failure is given by [26]:

$$\left(\frac{\mathcal{G}_I^i}{\mathcal{G}_{IC}^i}\right)^2 + \left(\frac{\mathcal{G}_{II}^i}{\mathcal{G}_{IIC}^i}\right)^2 = 1 \tag{15}$$

where $\mathcal{G}_I^i$ and $\mathcal{G}_{II}^{ii}$ are the dissipated fracture energies, given by:

$$\mathcal{G}_I^i(\mathfrak{d}) = \frac{1}{2} n_{t,0} g_n^2 \frac{g_{nc,0}^2}{\left[(1-\mathfrak{d}) g_{nc,0} + \mathfrak{d} g_{nc,1}\right]^2}, \tag{16a}$$

and

$$\mathcal{G}_{II}^i(\mathfrak{d}) = \frac{1}{2} k_{t,0} g_t^2 \frac{g_{tc,0}^2}{\left[(1-\mathfrak{d}) g_{tc,0} + \mathfrak{d} g_{tc,1}\right]^2} \tag{16b}$$

Furthermore, the critical fracture energies $\mathcal{G}_{IC}^i$ and $\mathcal{G}_{IIC}^i$ are:

$$\mathcal{G}_{IC}^i = \frac{1}{2} g_{nc,0}^2 k_{n,0}, \tag{17a}$$

and

$$\mathcal{G}_{IIC}^i = \frac{1}{2} g_{tc,0}^2 k_{t,0} \tag{17b}$$

2.3. Weak form of the variational problem

The weak forms of the phase field approach for the bulk and the cohesive zone model for the interfaces are herein detailed. The energy functional given in Eq. (5) is perturbed to arrive at the Galerkin's weak formulation. Considering the variation of the bulk energy functional in Eq. (6) with respect to the displacements u and the

phasefield variable $\mathfrak{d}$ yields:

$$\begin{aligned}\delta\Pi_b\left(\mathbf{u},\delta\mathbf{u},\mathfrak{d},\delta\mathfrak{d}\right) = &\int_\Omega \sigma : \delta\varepsilon \mathrm{d}\Omega - \int_\Omega 2\left(1-\mathfrak{d}\right)\delta\mathfrak{d}\psi_+^e\left(\varepsilon\right)\mathrm{d}\Omega \\ &+ \int_\Omega \mathcal{G}_c^b l\left[\frac{1}{l^2}\mathfrak{d}\delta\mathfrak{d} + \nabla_{\mathbf{x}}\mathfrak{d}\cdot\nabla_{\mathbf{x}}\left(\delta\mathfrak{d}\right)\right]\mathrm{d}\Omega + \delta\Pi_{b,\mathrm{ext}}\left(\mathbf{u},\delta\mathbf{u}\right)\end{aligned} \tag{18}$$

where, $\delta\mathrm{u}\in\mathfrak{V}^u = \left\{\delta\mathrm{u}|\mathrm{u}=\bar{\mathrm{u}}\text{ on }\partial\Omega_u,\ \mathrm{u}\in\mathcal{H}^1\right\}$ is the displacement test function, and $\delta\mathfrak{d}\in\mathfrak{V}^{\mathfrak{d}} = \left\{\delta\mathfrak{d}|\delta\mathfrak{d}=0\text{ on }\Gamma_b,\ \mathfrak{d}\in\mathcal{H}^0\right\}$ is the damage test function. The contribution of external forces in the variation of the bulk energy functional results in:

$$\delta\Pi_{b,\mathrm{ext}}\left(\mathbf{u},\delta\mathbf{u}\right) = \int_{\partial\Omega}\bar{\mathbf{t}}\cdot\delta\mathbf{u}\mathrm{d}\partial\Omega + \int_\Omega \mathbf{f}_v\cdot\delta\mathbf{u}\mathrm{d}\Omega. \tag{19}$$

Considering the variation of interface energy (Π_{Γ_i}) in Eq. (5) leads to:

$$\delta\Pi_{\Gamma_i}(\mathrm{u},\delta\mathrm{u},\mathfrak{d},\delta\mathfrak{d}) = \int_{\Gamma_i}\left(\frac{\partial\mathcal{G}^i(\mathrm{u},\mathfrak{d})}{\partial\mathrm{u}}\delta\mathrm{u} + \frac{\partial\mathcal{G}^i(\mathrm{u},\mathfrak{d})}{\partial\mathfrak{d}}\delta\mathfrak{d}\right)\mathrm{d}\Gamma\ ,\forall\ \delta\mathrm{u},\delta\mathfrak{d} \tag{20}$$

where the displacement test functions corresponding to the displacement field and to the phase field variable are defined in close analogy with the formulation for the bulk.

A numerical strategy provided in [25] is adopted here to solve the simultaneous quasi-static evolution problems for brittle fracture in the bulk and cohesive fracture along the pre-existing interfaces. Standard lower order finite elements are used for the spatial discretization, where a fully monolithic coupled solution scheme for the displacement and the phase field nodal variables is considered. Both bulk phase field elements as well as coupled-cohesive elements are modeled within four node iso-parametric finite element formulation.

3. Numerical Examples

In this section, crack propagation across the interfaces in composite materials has been studied considering varying geometric parameters using the developed hybrid PF-CZM method. The composites considered in this study are assumed to be laminated (fiber-matrix) types. In other words, laminae made of constituent2 and oriented in different directions are joined together using the constituent1. Therefore, laminated composite materials will consist of several interfaces. With an objective to capture the interfacial crack growth, five different types of specimen: single layer, bi-layer, tri-layer, multi-layer and woven composite cases were simulated. All the specimens are two dimensional in nature, subjected to uni-axial tensile test. The simulations are continued until the crack reaches the opposite boundary and the specimen separates into two parts.

Crack patterns in the composites are observed to be complex with delamination along the interfaces. The developed methodology enables capturing such complexities illustrated through different specimens mentioned above. In Section 3.1, brittle crack growth in a single material subjected to an uni-axial tensile test of a flat single-edge notched specimen made of a homogeneous material is studied. In Section 3.2, crack growth in a bi-material, where the layers are joined by an interface with varying properties has been studied. The interface properties are varied by changing their fracture toughness and the other parameters are derived accordingly. Crack propagation in triple and multiple layered composites are studied in Sections 3.3 and 3.4, respectively. A new modeling approach is developed to study the effect of spacing of constituent2 on fracture toughness of composite laminate as the crack grows. Therefore, the influence of constituent2 spacing in a composite laminate is studied in Section 3.5. The crack propagation in a unidirectional composite laminate when subjected to transverse loading is discussed in Section 3.6. Crack propagation in woven composite laminate is studied in Section 3.7. To summarise, crack growth across the perfectly bonded interfaces (without any interface) and the presence of interface between the materials 1 and 2 in the above specimens when loaded in mode I has been thoroughly investigated.

3.1. Numerical example 1: crack growth in homogeneous single-edge notched specimen

The proposed hybrid PF-CZM method is first applied to simulate the crack growth in a flat single-edge notched specimen under uniform tensile loading as shown in Fig. 4. The material parameters of the specimen are mentioned in Table 1. The dimensions of the specimen are 1×1 mm^2. The domain is discretized using 4-noded QUAD elements. The total number of elements are observed to be 10050, with 10506 number of nodes. An initial edge notch of size 0.5 mm is introduced at 0.5 mm from the bottom surface, see Fig. 4. A displacement load of 0.0001 mm per cycle is specified on to the top and bottom edges of specimen.

The cumulative displacement and the reaction forces at every load step are calculated. The deformed configurations considering a fracture energy of 2.7 N/mm, at cumulative displacements of 0.0062 mm, 0.008

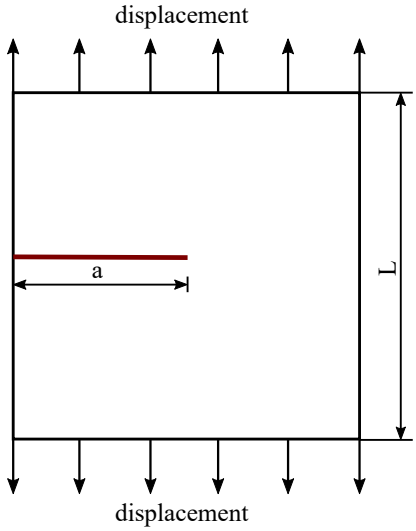

Figure 4: Schematic of a homogeneous two dimensional specimen containing an edge crack.

Lame's constants		Fracture energy
λ (kN/m^2)	μ (kN/m^2)	G_c (N/mm)
121.15	80	2.7

Table 1: Material properties of the specimen in Fig. 4.

mm, and 0.0096 mm are shown in Figs. 5(a), (b) and (c), respectively. The crack is observed to grow when the displacement reaches 0.0062 mm, see Fig. 5(a), and continue to grow with increased displacement. The material is observed to be separating into two parts at a displacement of 0.0096 mm.

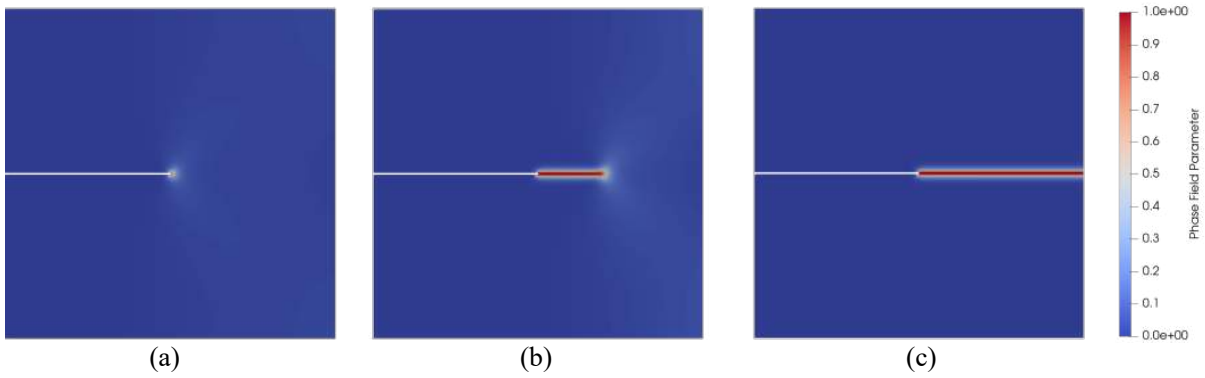

Figure 5: Crack growth studies in a single edge notched specimen. Deformed configurations highlighting the phase field parameter when the cumulative displacement is equal to (a) 0.0062 mm, (b) 0.008 mm and (c) 0.0096 mm.

Furthermore, the studies are extended considering fracture energies of 5.4 N/mm and 8.1 N/mm. A plot of the reaction force vs. displacement for different fracture energies and characteristic lengths are shown in Figs. 6(a) and (b), respectively. According to Fig. 6(a), the peak force is observed to increase with increase in fracture energy. The peak force indicates the deformed configuration, where the material separates into two parts. According to Figs. 6(a) and (b), the initial response of the specimen varies in a linear fashion. As the damage starts to accumulate, indicated by the increase in phase field parameter ahead of the crack tip, the force-displacement curve is observed to become non-linear. After reaching the critical energy release rate G_c, the initial crack propagates rapidly. Even though there is still an increase in the applied load, the material starts losing its load-bearing capacity, and a sharp drop is observed.

Therefore, when the fracture energy is equal to 2.7 N/mm, the corresponding displacement at fracture is found to be 0.0096 mm, which in agreement with the results published in [31]. The influence of characteristic length (l_c) can be observed from Fig. 6(b). Figure 6(b) shows the traction displacement plots considering characteristic lengths of 0.0025 mm, 0.005 mm and 0.0075 mm. The peak force in Fig. 6(b) is observed to be increasing with decreasing value of l_c, the length scale parameter that controls the spread of the damage. As l_c tends to 0, sharp solution limit is approached. The increase in force is the result of an increase in the apparent strength.

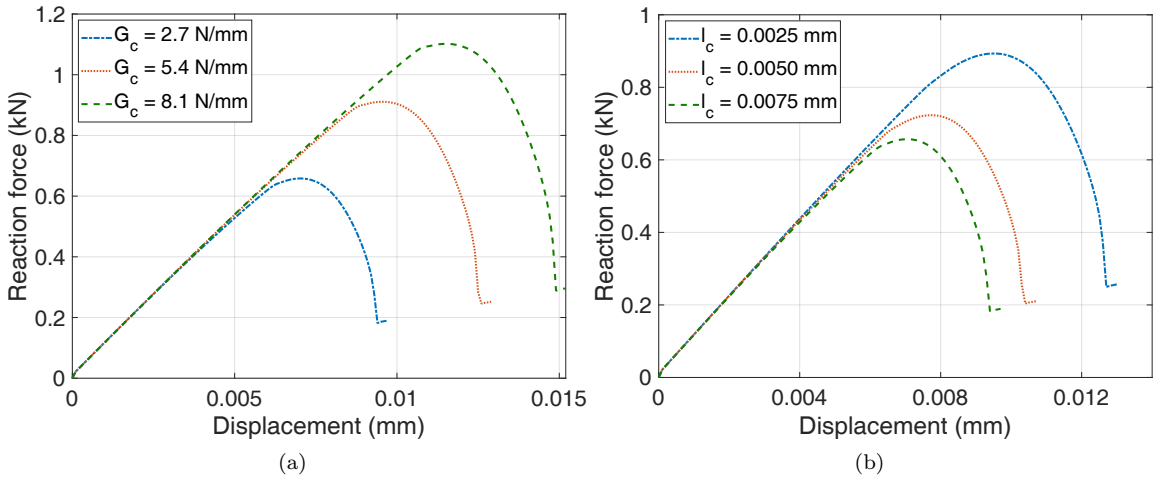

Figure 6: Comparison of traction-displacement curves for the specimen shwon in Fig. 4, considering (a) fracture energies equal to 2.7 N/mm, 5.4 N/mm, and 8.1 N/mm and (b) characteristic lengths equal to 0.0025 mm, 0.005 mm, and 0.0075 mm.

3.2. Numerical example 2: crack propagation in single-edge notched bi-material specimen

In this example, crack propagation in a single-edge notched bi-material specimen is studied. The specimen is made of two layers of the same material, where they are either perfectly bonded or joined through an interface. The orientation of the interface is assumed to be perpendicular to the crack axis and runs along the length of the specimen as shown in Fig. 7. The interface material is discretized using the coupled cohesive-phase field elements.

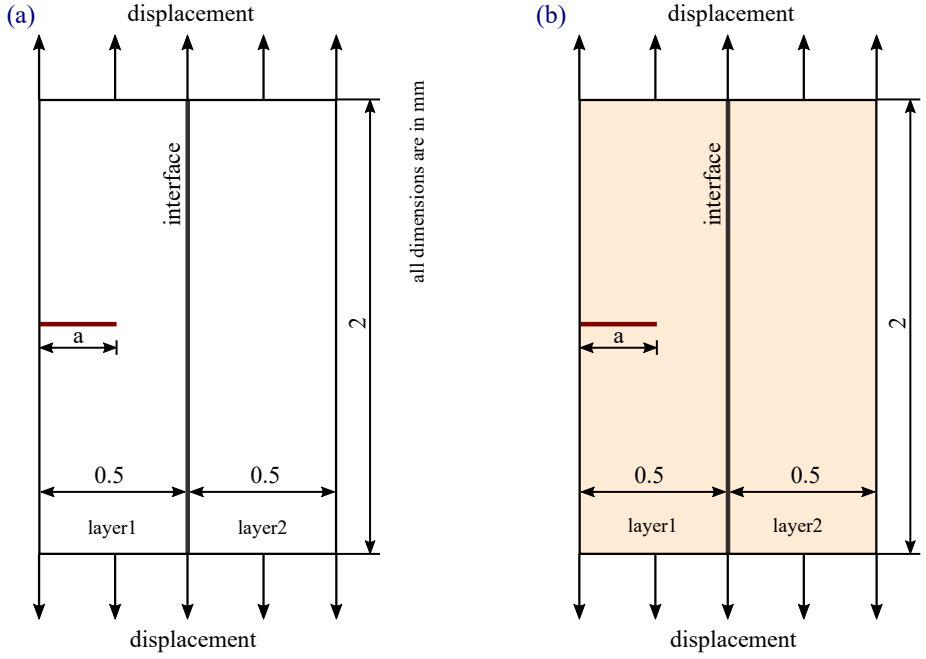

Figure 7: Schematic of a single-edge notched bi-material specimen with an interface, when the initial edge crack is contained in the (a) constituent1 and (b) constituent2 respectively.

The mechanical properties of the constituent1 and constituent2 used in the simulations are listed in Table 2, whereas, the fracture properties of the interface are shown in Table 3. Critical fracture energies of the interface listed in Table 3 corresponds to a brittle and tough interface at a constant critical stress (σ_c) of 2[1] GPa. The corresponding values of critical normal opening ($g_{nc,0}$) and initial stiffness ($k_{nc,0}$) are also listed in Table 3. Therefore, based on the values in Table 3, a brittle interface is observed to posses a small normal opening and high initial stiffness as compared to the tough interface. In order to study the influence of material properties,

[1]In simulations, the parameters used model the interfaces are derived at constant initial peak stress of 2 GPa. The corresponding parameters for a tough interface are: $\sigma_{c,0}$, $\tau_{c,0}$ = 2 GPa and k_0, the initial stiffness is 0.8 MPa/mm with a critical normal crack opening distance of 0.0025 mm. Similarly the parameters for the brittle interface are: $\sigma_{c,0}$, $\tau_{c,0}$ = 2 GPa and the initial stiffness of interface is 80 MPa/mm with a critical normal crack opening distance of 0.000025 mm.

simulations are performed considering three different cases based on the method of joining of two parts of the bi-material composite: (i) perfectly bonded, and bonded using an interface material of critical fracture energy (ii) 0.025 N/mm and (iii) 2.5 N/mm, see Table 3.

Material	Young's modulus (GPa)	Poisson's ratio	Fracture energy (N/mm)	Characteristic length (mm)
constituent1	70	0.34	0.025	0.075
constituent2	300	0.14	0.005	0.075

Table 2: Mechanical properties of the materials of materials 1 and 2 considered in this study [25].

Case	Critical fracture energy (G_c^i) (N/mm)	Critical normal opening ($g_{nc,0}$) (mm)	Critical stiffness ($k_{\mathrm{nc},0}$) (N/mm^3)
1	0.025	2.5×10^{-5}	80×10^6
2	2.5	2.5×10^{-3}	80×10^4

Table 3: Critical fracture properties of the interface material adopted in the simulations.

In the numerical simulations, the height of the domain (see Fig. 7) is adopted as 2 mm, whereas the width of each layer is assumed to be 0.5 mm and the interface is modelled as a 0.005 mm thick material. The discretised domain is found to contain 11421 elements with 12763 nodes in total. An initial crack of size 0.25 mm is introduced in the middle of the first domain, see Fig. 7. The simulations are performed by specifying a displacement load of 0.00005 mm per cycle on to the top and bottom edges of the specimen (see Fig. 7) until the specimen fractures into two parts.

3.2.1. Case 1: Crack in the constituent of bi-layer composite

The two layers of the bimaterial specimen are assumed to be made of constituent1, see Fig. 7(a) and Tables 2 and 3. Simulations are performed considering an interface material of fracture energy equal to 0.025 N/mm. The first row of Fig. 8 shows the distribution of phase field parameter in the deformed configurations of the bimaterial specimen, at cumulative displacements loads equal to 0.001 mm, 0.0015 mm, 0.002 mm, 0.0025 mm and 0.00305 mm. According to the deformed configurations in Figs. 8(a-e), the crack is observed to grow along its axis until meeting the interface material, where it has traversed along the interface in the loading direction before entering the second part of the bimaterial. The traversing has happened because of the differences in elastic modulus of the constituent1 and interface materials. The specimen is observed to fracture after some propagation in the second part of the bimaterial. Similarly, crack propagation in the bi-material assuming both parts are perfectly bonded are shown in Figs. 8(f-j). The absence of interface has allowed the crack to pass through the joint without traversing.

Traction-displacement curves for brittle, tough and no interface cases are shown in Fig. 9(a). Based on Fig. 9(a), the crack propagation in all the three cases is observed to follow a similar trend. This implies that for the given geometric parameters, interface material do not have any influence on the crack propagation.

3.2.2. Case 2: Crack in the constituent2 of bi-layer composite

In this case, the two layers of the bimaterial specimen are made of constituent2, see Fig. 7(b) and Tables 2 and 3. With an objective to study the crack growth, simulations are repeated under the similar conditions discussed in Section 3.2.1. Since constituent2 is more brittle as compared to constituent1, the crack velocity is expected to be higher in this case. Therefore, when the specimen is loaded in mode I, crack is observed to reach the interface faster than case 1.

The distribution of the phase field parameter during the deformation of bi-material specimen is shown in Fig. 10. The deformed configurations are captured when the cumulative displacement is equal to 0.00015 mm, 0.0004 mm, 0.00255 mm, 0.0033 mm and 0.345 mm. The top row Figs. 10(a-e) indicates the deformed configuration of the bi-material specimen where the two parts are joined through an interface having the fracture energy equal to 0.025 N/mm. Upon the application of the displacement load the crack is observed to grow along its axis in the first part of the bi-material, where it is observed to traverse along the interface in the loading direction before entering the second part of the bi-material, see Figs. 10(a-e). This is in agreement with the results published in [26]. The crack can travel along the interface until the ratio of critical fracture energy of interface to the critical fracture energy of constituent2 in the current load step is less than the critical value. When the ratio exceeds a critical value the crack penetrates into the second part of the material, see Fig. 10. A similar trend is observed when the simulations were repeated with a tough interface having fracture energy equal to 2.5 N/mm.

The simulations are repeated assuming that both parts of the bi-material are perfectly bonded without any interface. The bottom row Figs. 10(f-j) indicate the corresponding deformed configurations when the

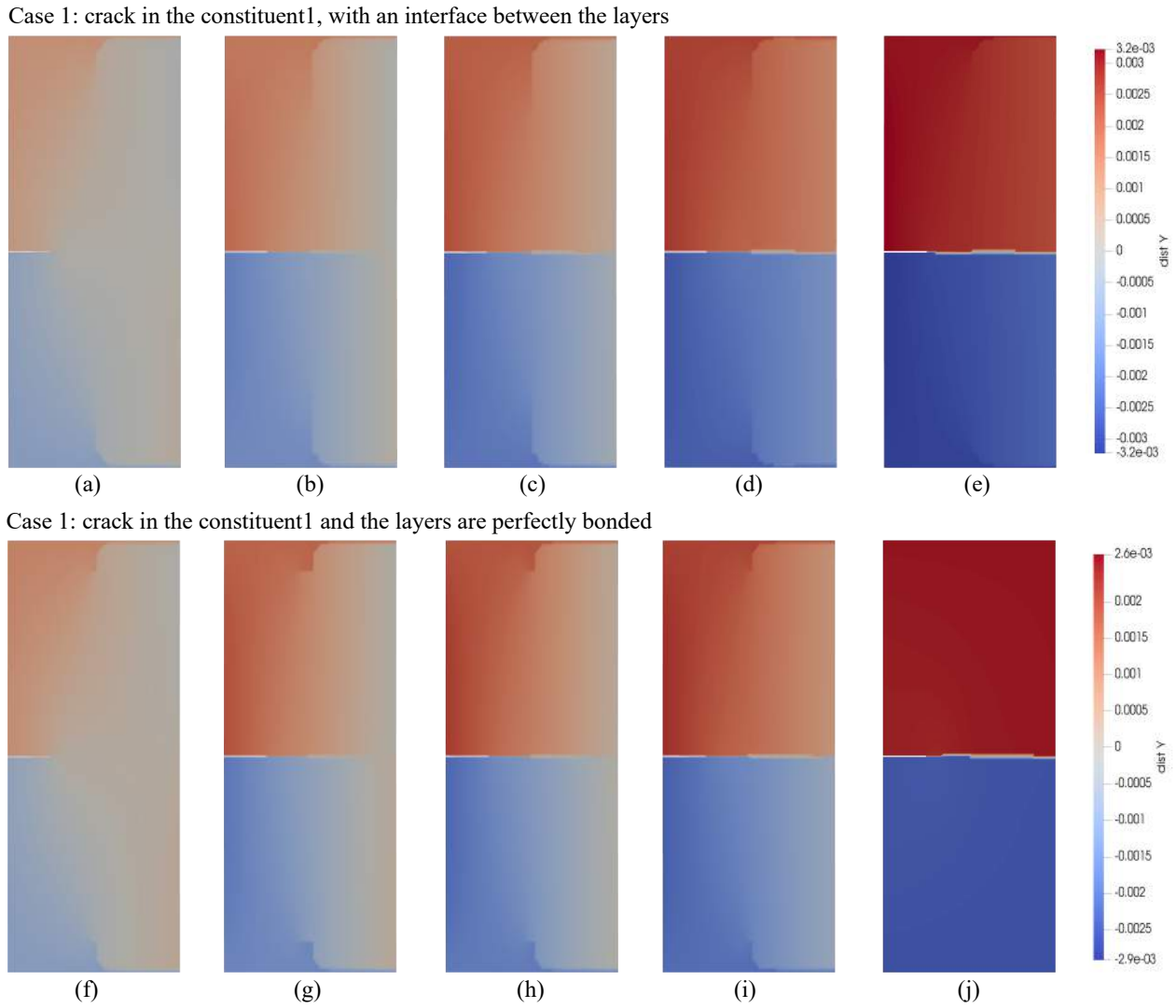

Figure 8: Crack in the constituent1: distribution of displacement along the y direction of the bi-material specimen made of two layers of constituent1, see Fig. 7(a). The top row indicates the configuration with an interface of fracture energy equal to 0.025 N/mm at applied displacements equal to (a) 0.001 mm, (b) 0.0015 mm, (c) 0.002 mm, (d) 0.0025 mm and (e) 0.00305 mm. The corresponding configurations assuming a perfect bonding between the two layers at applied displacements equal to (f) 0.001 mm, (g) 0.0015 mm, (h) 0.00175 mm, (i) 0.002 mm and (j) 0.0025 mm are shown in the bottom row.

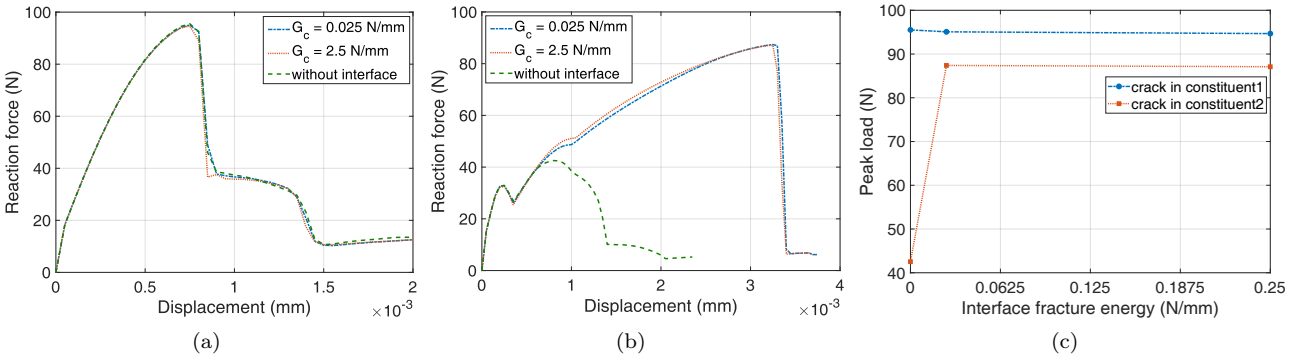

Figure 9: Variation of the traction with displacement considering that the bi-material composite is perfectly bonded and joined through an interface fracture energy equal to 0.025 N/mm and 2.5 N/mm, assuming that both layers are made of: (a) constituent1 and (b) constituent2 alone. The peak loads for the cases in (a) and (b) are plotted in (c). A perfectly bonded interface is identified by zero fracture energy of the interface.

cumulative displacement is equal to 0.00015 mm, 0.0004 mm, 0.00255 mm, 0.0033 mm and 0.345 mm. The fracture toughness of the perfectly bonded bi-material is observed to be less than that of bi-material specimen joined through an interface. This is attributed to the fact that the interface helps to transfer the loads across the two layers of the composite through shear transfer. Such load transfer will be absent when the two layers are

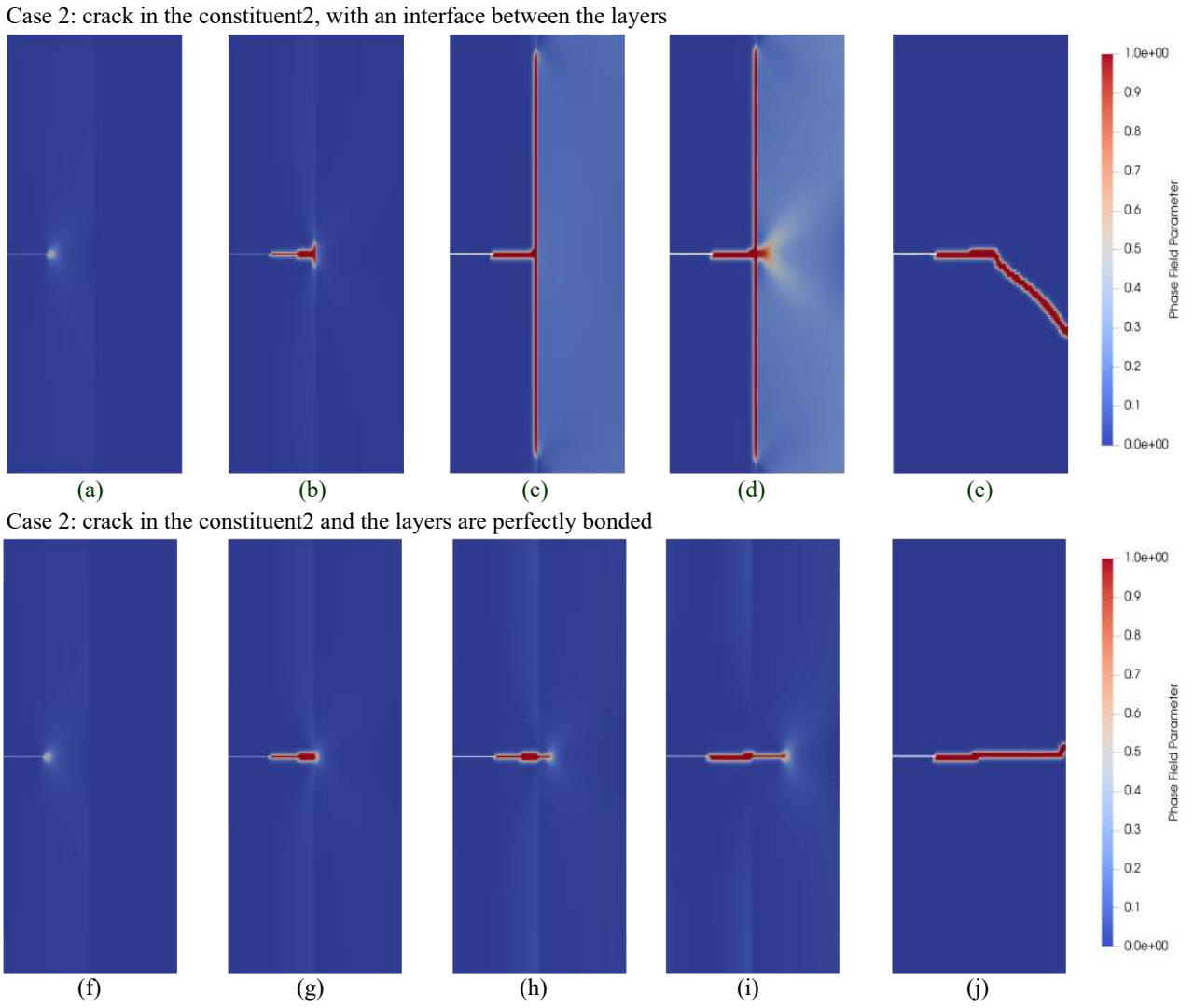

Figure 10: Crack in the constituent2: distribution of phase field parameter in the deformed configuration of bi-material specimen made of two pieces of constituent2, see Fig. 7(b). The top row indicates the configuration with an interface of fracture energy equal to 0.025 N/mm at applied displacements equal to (a) 0.00015 mm, (b) 0.0004 mm, (c) 0.00255 mm, (d) 0.0033 mm and (e) 0.00345 mm. The corresponding configurations assuming a perfect bonding between the two patches at displacement load equal to (f) 0.00015 mm, (g) 0.00045 mm, (h) 0.0007 mm, (i) 0.001 mm and (j) 0.00225 mm are shown in the bottom row.

perfectly joined. The load-displacement variation considering perfectly bonded and joined through an interface of fracture energies equal to 0.025 N/mm and 2.5 N/mm are shown in Fig. 9(b). A comparison of Figs. 9(a) and (b) indicates that the displacement at fracture is more in case 2 compared to case 1. However, the peak load in case 1 is higher compared to case 2, see Fig. 9(c). Furthermore, the peak loads in case 1 is observed to be constant irrespective of the interface. Whereas, the constituent2 made bimaterial with perfectly bonded layers fails much faster (see Fig. 9(b)) compared to the other two cases. The absence of interface in a brittle constituent2 phase makes the composite totally brittle. Therefore, the crack is observed to smoothly enter the second part after a small jump across the interface. This jump was ironed out after some crack propagation in the second part, see Figs. 10(f-j). As a result, the peak loads in constituent2 made composite are observed to increase with increased fracture energy of the interface from 0 to 2.5 N/mm, see Fig. 9(c). To summarize, crack propagation in the composite made of constituent2 is close to brittle fracture.

3.3. Numerical example 3: crack propagation in single-edge notched tri-layer specimen

In this example, the composite material is made of three layers as shown in Fig. 11, where the materials of three layers are: constituent1, constituent2 (identified as the shaded region) and constituent1, respectively. The height of the domain is adopted as 3 mm, whereas, width of each layer along the x direction is equal to 0.5 mm, 0.25 mm and 0.25 mm, and the thickness of each interface is equal to 0.005 mm, such that the total width of the specimen is equal to 1.01 mm, see Fig. 11. The domain is discretized using 4-noded QUAD elements, where the total number elements are found to be 17342 containing 19979 nodes. The critical strength of the interface material (σ_c) is considered as 2 GPa in all the simulations. The influence of interface on crack propagation is

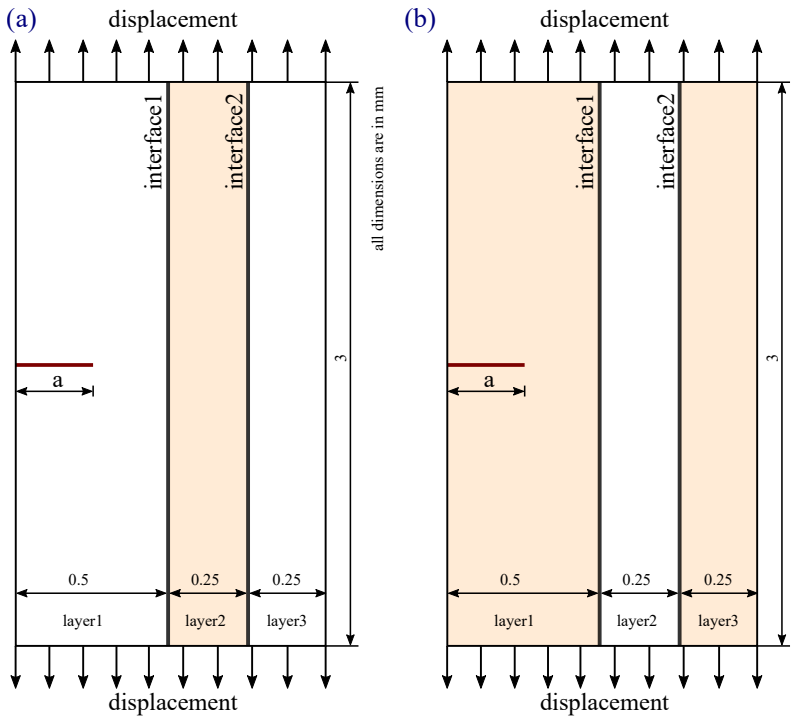

Figure 11: Tri-layer single-edge notched specimen used in the simulations. Sub-figures (a) and (b) indicate the configurations when the crack is contained in the constituents 1 and 2, respectively.

studied through two different cases by altering the materials of the layers in Fig. 11. Therefore, this scenario is different from the cases discussed in Section 3.2 where the material of both layers are same.

3.3.1. Case 3: Crack in the constituent1 of tri-layer composite

An initial edge crack of size 0.25 mm is created in the constituent1 as shown in Fig. 11(a). Furthermore, the layer between the interfaces is made of constituent2, see Tables 2 and 3 for their properties. Three different composites, perfectly bonded layers without interface and joined by an interface having fracture energies of 0.025 N/mm and 2.5 N/mm are considered in the simulations. The composite specimen is subjected to uniaxial displacement load of 0.00005 mm per cycle.

Variation of the phase field parameter with deformation considering an interface of fracture energy equal to 0.025 N/mm when the applied displacements are equal to 0.0025 mm, 0.0028 mm, 0.0062 mm, and 0.0094 mm are shown in Figs. 12(a-d). Whereas, the corresponding pictures with a perfect bonding between the layers when the displacement load is equal to 0.0025 mm, 0.0027 mm, 0.0031 mm, and 0.0037 mm are shown in Figs. 12(e-h). The top row Figs. 12(a-d) indicate that the external load in the initial stages is resisted by the all the three layers until the edge crack starts to propagate. Since the fracture toughness of constituent2 is less than that of constituent1, cracks are observed to be initiating in constituent2 while they continue to grow in the constituent1, see Fig. 12(b). Upon continued loading cracks in the constituent1 and constituent2 were observed to travel parallel to each other until reaching the first interface. After the crack in constituent1 reaches the interface, it is observed to traverse along the interface along the axial direction to meet with the initiated cracks in the constituent2, see Fig. 12(c). Therefore, the deformed configuration appears like a branched crack at the first interface. As a result, with further loading the crack branches start to traverse along the second interface. In order to penetrate into the third layer the condition of crack penetration vs deflection along the interface has to be satisfied. The material separates into two parts after the crack penetrates into the last layer. However, when the layers are perfectly joined without any interface between them, due to the rigid nature of the interfaces, the crack will not deflect at the interfaces, see Figs. 12(e-h). However, crack branching is noticed before the fracture.

Variation of the reaction force with displacement is shown in Fig. 13(a), where the increase in fracture toughness of composite after the introduction of interface can be observed. This is because the interface helps to transfer the load through shear transfer and hence dissipates the stresses across the interface, see Fig. 12(c). Furthermore, as observed in Fig. 13(a) the reaction force is noticed to suddenly drop when the layers are joined without an interface, indicating the brittle failure.

3.3.2. Case 4: Crack in the constituent2 of tri-layer composite

In order to study the influence of the order of layers, crack propagation in the configuration shown in Fig. 11(b) was studied with and without the interface. Evolution of the phase field parameter with deformation is

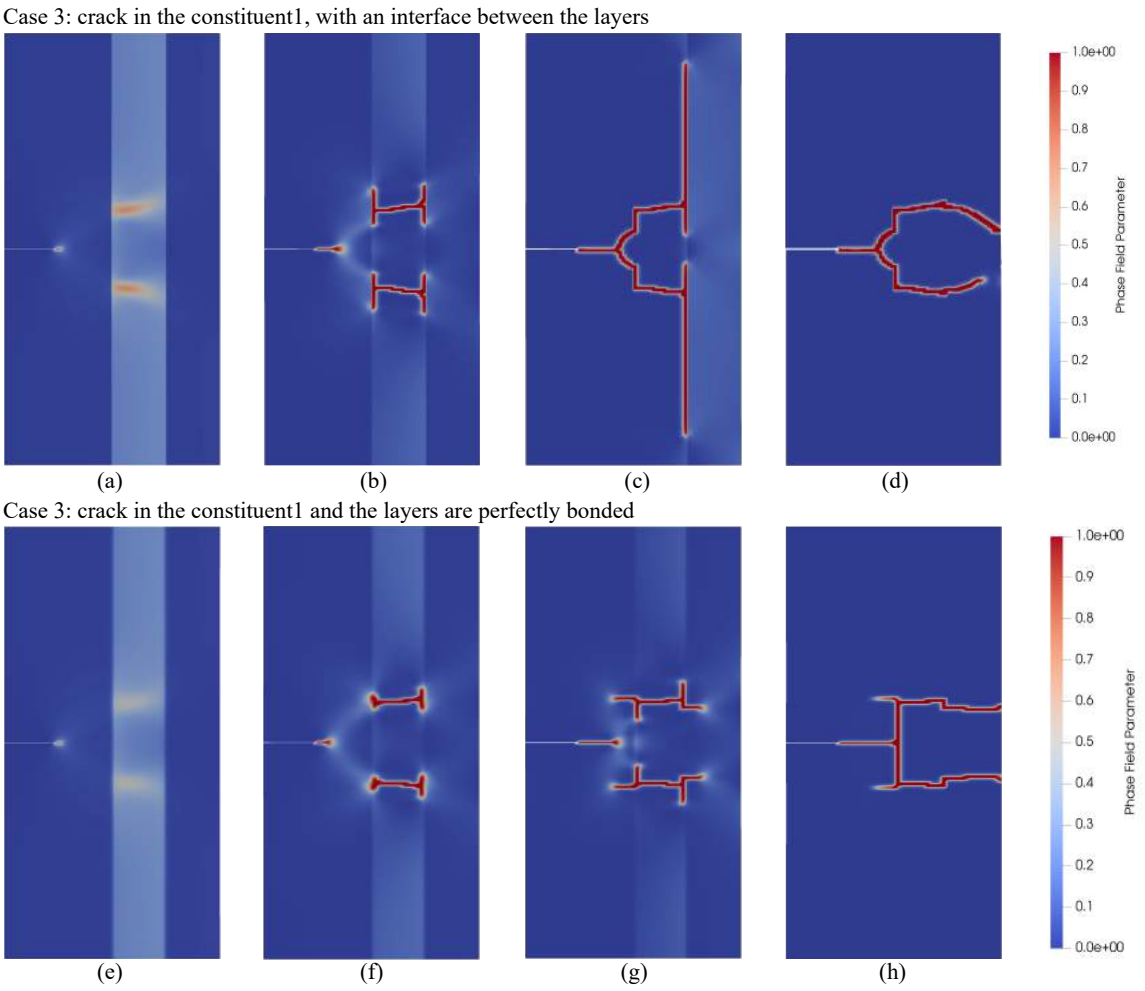

Figure 12: Crack in the constituent1: distribution of phase field parameter in the deformed configuration of tri-layer specimen shown in Fig. 11(a). The top row indicates the configuration with an interface of fracture energy equal to 0.025 N/mm at applied displacements equal to (a) 0.0025 mm, (b) 0.0028 mm, (c) 0.0062 mm, and (d) 0.0094 mm. The corresponding configurations assuming a perfect bonding between the layers at displacement load equal to (e) 0.0025 mm, (f) 0.0027 mm, (g) 0.0031 mm, and (h) 0.0037 mm are shown in the bottom row.

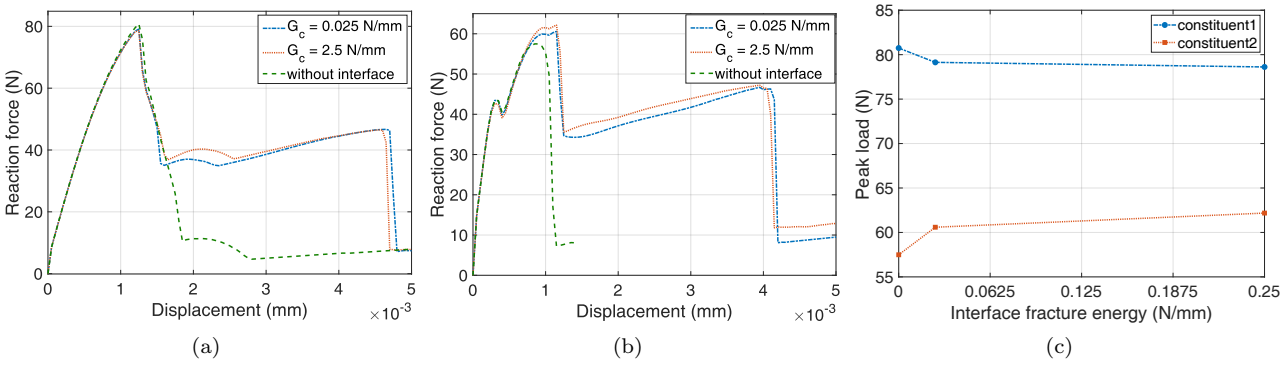

Figure 13: Comparison of the traction vs. displacement plots considering the tri-material composite when the layers are perfectly bonded and joined through interfaces of fracture energy equal to 0.025 N/mm and 2.5 N/mm, as described in (a) case 3 and (b) case 4. The peak loads for the cases in (a) and (b) are plotted in (c). A perfectly bonded interface is identified by zero fracture energy of the interface.

shown in Fig. 14. The top row Figs. 14(a-d) indicate the deformed configurations of the composite, whose layers are joined by an interface material of fracture energy equal 0.025 N/mm, corresponding to displacement loads of 0.0006 mm, 0.0023 mm, 0.007 mm and 0.0101 mm. The bottom row Figs. 14(e-h) represent the deformed configurations of the perfectly joined composite without any interface material, and corresponding to displacement loads of 0.0006 mm, 0.0017 mm, 0.0021 mm and 0.0027 mm.

The influence of altering the layer sequence is clear by comparing Figs. 12(a-d) and 14(a-d). Although the interface material is the same in both cases, the crack is clearly observed to deflect in second and third layers in

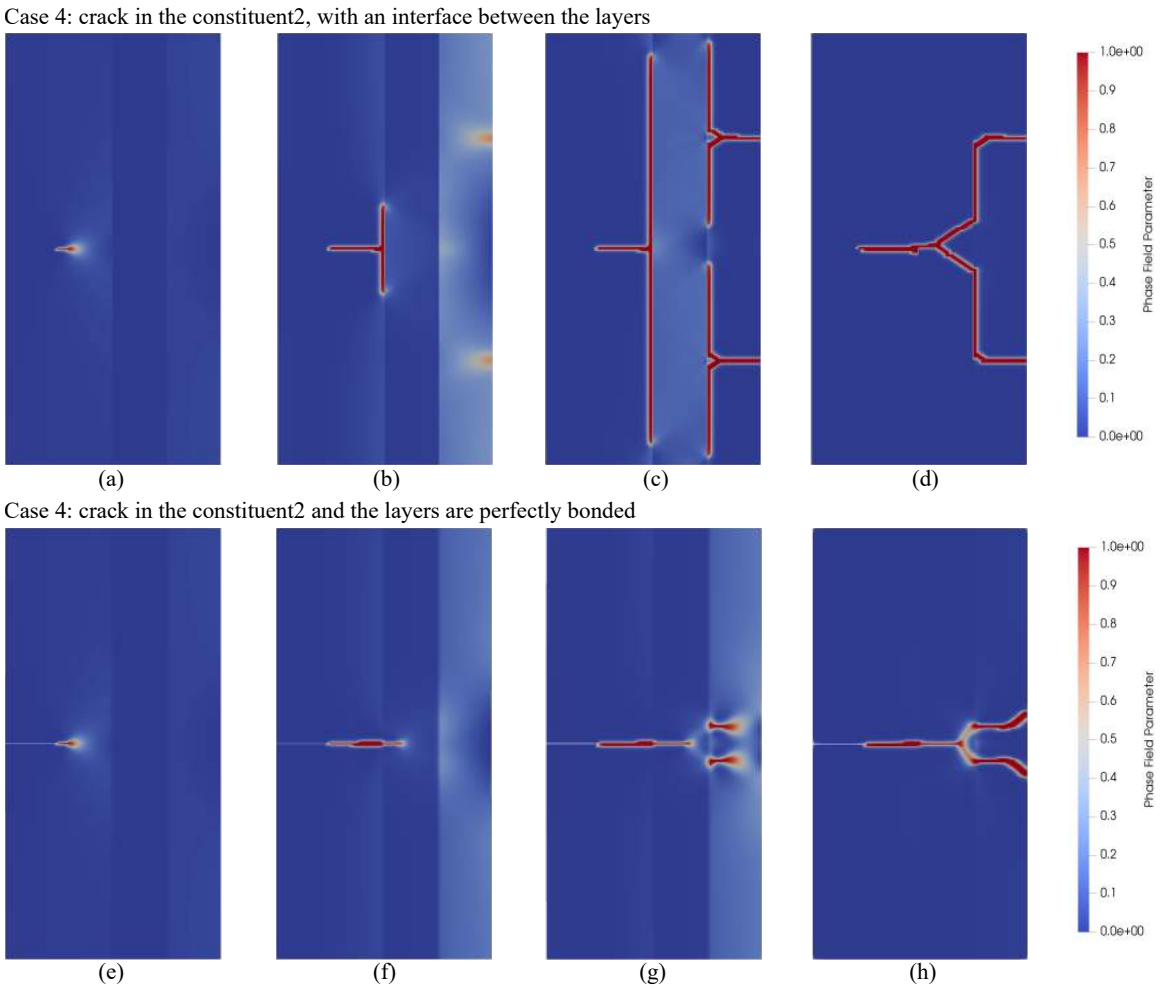

Figure 14: Crack in the constituent2: distribution of phase field parameter in the deformed configuration of tri-layer specimen shown in Fig. 11(b). The top row indicates the configuration with an interface of fracture energy equal to 0.025 N/mm at applied displacements equal to (a) 0.0006 mm, (b) 0.0023 mm, (c) 0.007 mm, and (d) 0.0101 mm. The corresponding configurations assuming a perfect bonding between the layers at displacement load equal to (f) 0.0006 mm, (f) 0.0017 mm, (g) 0.0021 mm, and (h) 0.0027 mm are shown in the bottom row.

the later case. The difference in stiffness of constituents 1 and 2 is the main reason for crack deflection. In case 4, the crack starts its propagation in a stiff constituent2, which requires higher fracture energy as compared to case 3, where the crack initially starts its propagation in the soft constituent1. Therefore, the total load is shared by the constituent2 in case 4, until reaching the interface. Simultaneously, due to its low stiffness, constituent1 continue to elongate until the crack completely propagates through the constituent2. The interface helps in constituent1 elongation by distributing the load between constituent2 and constituent1 through shear transfer. Therefore, the crack is observed to traverse along the interface soon after arriving at the interface. The traversing is continued until the sliding at the second interface between constituent1 and constituent2 leads to constituent2 pull-out through initiation of cracks in the third layer, i.e. constituent2 layer, see Fig. 11(b). As a result, the fracture is observed to happen though crack branching, see Fig. 14(d). On the other hand, when the interfaces are perfectly joined without any interface crack deflection is totally absent, as shown in Figs. 14(e-h). Therefore, the crack is observed to simply transit from one layer to another during its propagation. Absence of shear transfer due to the absence of interface is the main reason for this behavior.

Variation of the reaction forces vs. displacement for case 4 is shown in Fig. 13(b), where the fracture toughness is found to be significantly higher in the presence interface. Furthermore, the crack deflection at the interface is evident through a load drop around a cumulative displacement of 0.0012 mm, see Figs. 14(b) and 13(b). A comparison of the peak loads in cases 3 and 4 is provided in Fig. 13(c), where the maximum load in case 3 is observed to be higher than that of case 4 for the given range of displacement. This infers that composite in case 3 absorbs higher energy as compared to the composite in case 4. This is expected since the total area of brittle constituent2 in cases 3 and 4 is equal to 25% and 75%, respectively. Therefore, the fracture toughness of the composite with layer sequence in case 3 is higher as compared to the composite with layer sequence in case 4.

3.4. Numerical example 4: crack propagation in single-edge notched six-layer specimen

The composite in this example is made of six alternating layers of constituent1 and constituent2. Therefore, this can be considered as an extension of numerical example 3 discussed in Section 3.3. A schematic of the multi-layered composite containing an edge crack is shown in Fig. 15. The length of domain is adopted to be 6 mm, width of layer1 is equal to 0.5 mm and that layers 2 to 6 is equal to 0.25 mm, and the width of the interface is equal to 0.005 mm, see Fig. 15. The domain in discretized with 4-noded QUAD-elements yielding a total of 18065 elements with 22907 nodes. Considering the critical stress of the interface (σ_c) as 2000 MPa, the influence of interface on crack propagation is studied through cases 5 and 6, discussed in Sections 3.4.1 and 3.4.2, respectively.

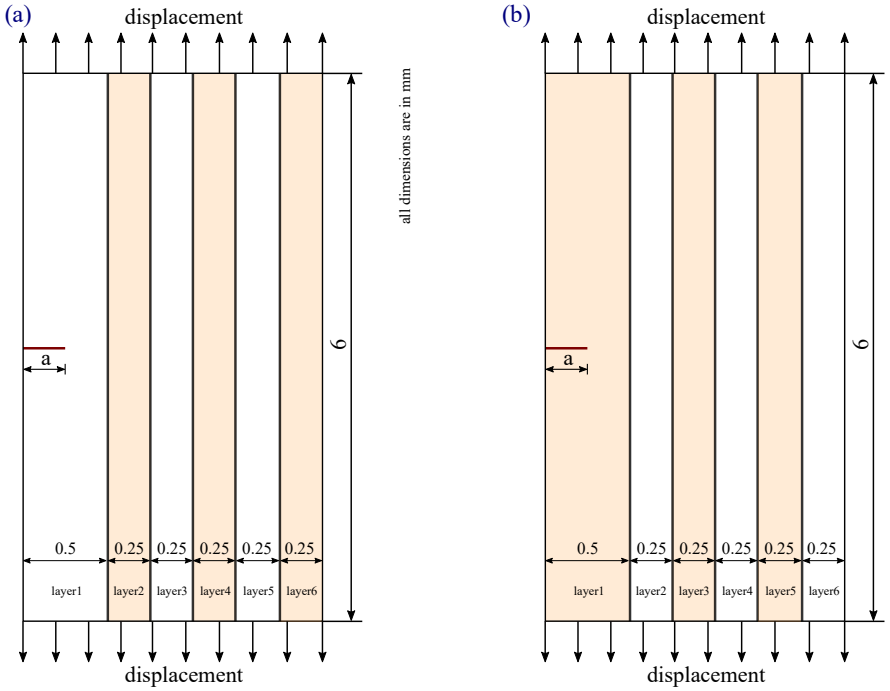

Figure 15: Six-layered single-edge notched composite specimen used in the simulations. Configurations in (a) and (b) indicates that the crack is contained in the constituents 1 and 2, respectively.

3.4.1. Case 5: Crack in the constituent1 of multi-layer composite

In order to study the influence of number and order of layers, crack propagation in the six layered composite is shown in Fig. 15(a) was studied with and without the interface. As shown in Fig. 15(a), the crack is contained in the constituent1.

The evolution of the phase field parameter with deformation is shown in Fig. 16. The top row Figs. 16(a-e) indicate the deformed configurations of the composite, whose layers are joined by an interface material of fracture energy equal 0.025 N/mm, corresponding to displacement loads of 0.0064 mm, 0.0067 mm, 0.0068 mm, 0.01465 mm and 0.01485 mm. Whereas, the bottom row Figs. 16(f-j) represent the corresponding deformed configurations of the perfectly bonded composite without any interface material, at the applied displacement levels equal to 0.00335 mm, 0.00345 mm, 0.00355 mm, 0.00375 mm and 0.00435 mm. On the other hand, evolution of the phase field parameter with deformation is shown in Fig. 17. The pictures in Fig. 17 indicate the deformed configurations of the composite, whose layers are joined by an interface material of fracture energy equal 2.5 N/mm, corresponding to displacement loads of 0.00448 mm, 0.00469 mm, 0.00476 mm, 0.014 mm and 0.01505 mm.

As the fracture toughness of constituent1 is more than that of constituent2, cracks are observed to initiate in multiple layers of constituent2 simultaneously, while the main crack in the constituent1 in layer1 continue to grow, see Fig. 16(b). Upon continued loading cracks in the constituent1 and constituent2 were observed to grow parallel to each other until reaching the interfaces. The main crack in the constituent1 layer is observed to join the constituent2 cracks when the displacement load is equal to 0.0068 mm, see Fig. 16(c). However, it is observed that the constituent1 crack do not has scope to traverse along the loading direction after reaching the interface. This is because the locations of constituent2 cracks is close to the main crack, see Fig. 16(c). Therefore, the deformed configuration appears like a branched crack at the first interface. Further increase in the applied load is observed to be dissipated through shear transfer by the interface, resulting in crack growth at the interfaces along the loading direction, see Fig. 16(d). Finally, the material separates into two parts after crack penetration into the last layer, see Fig. 16(e). On the other hand, when the layers are perfectly joined

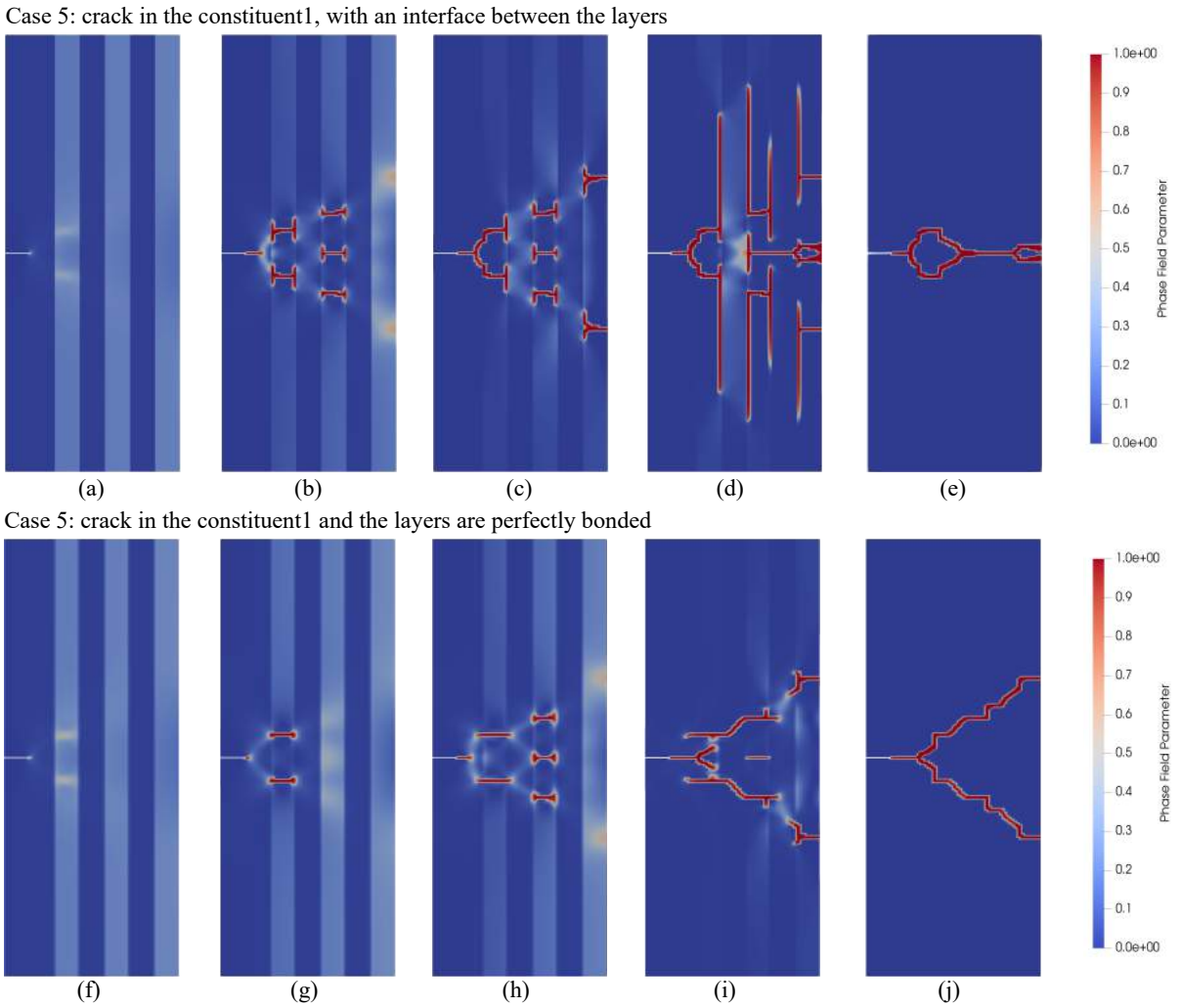

Figure 16: Crack in the constituent1: distribution of phase field parameter in the deformed configuration of a six layered specimen shown in Fig. 15(a). The top row indicates the configuration with an interface of fracture energy equal to 0.025 N/mm at applied displacements equal to (a) 0.0064 mm, (b) 0.0067 mm, (c) 0.0068 mm, (d) 0.01465 mm and (e) 0.01485 mm. The corresponding configurations assuming a perfect bonding between the layers at displacement load equal to (f) 0.00335 mm, (g) 0.00345 mm, (h) 0.00355 mm, (i) 0.00375, and (j) 0.00435 mm are shown in the bottom row.

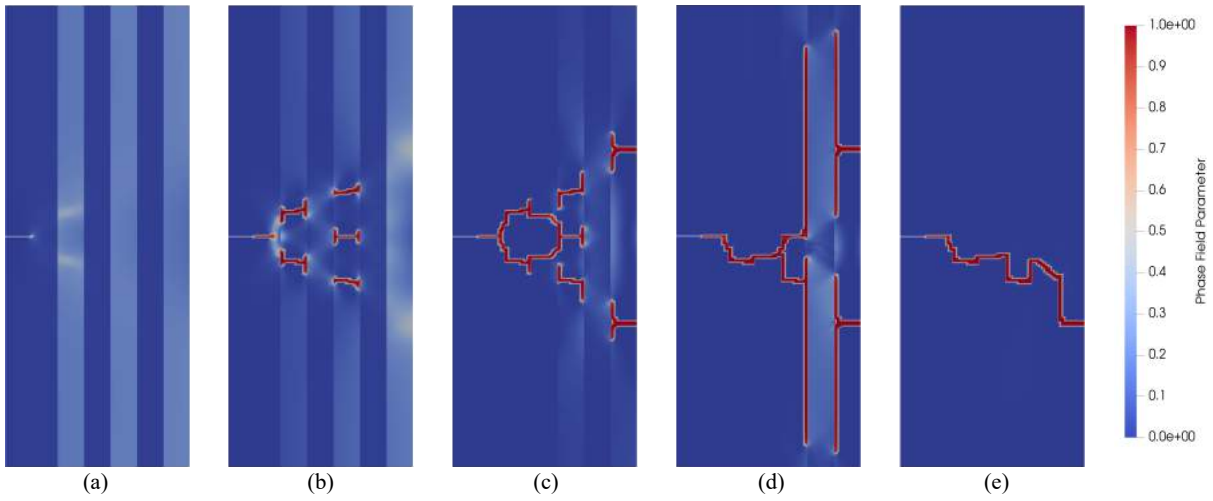

Figure 17: Crack in the constituent1: distribution of phase field parameter in the deformed configuration of a six layered specimen shown in Fig. 15(a). The pictures indicate the configuration with an interface of fracture energy equal to 2.5 N/mm at applied displacements equal to (a) 0.00448 mm, (b) 0.00469 mm, (c) 0.00476 mm, (d) 0.014 mm and (e) 0.01505 mm.

without any interface between them, the composite is observed to behave as a brittle material. Because of the rigid nature of the interfaces, the initiated cracks in the constituent2 layers were observed to join at the

interfaces without much deflection, see bottom row pictures of Fig. 16. The over all crack growth appears like a branching of the main crack, see Fig. 16(e).

Variation of the reaction force with displacement is shown in Fig. 18(a), where the increase in fracture toughness of composite after the introduction of interface with fracture energy 0.025 N/mm can be observed. The interface composite is observed to be tending to a perfectly bonded composite with increase in fracture energy of the interface, see Fig. 18(a). This is because with increased number of layers more cracks are observed to be simultaneously generated in the brittle constituent2 close to the main crack, there by scope for load transfer across the interface through shear reduces.

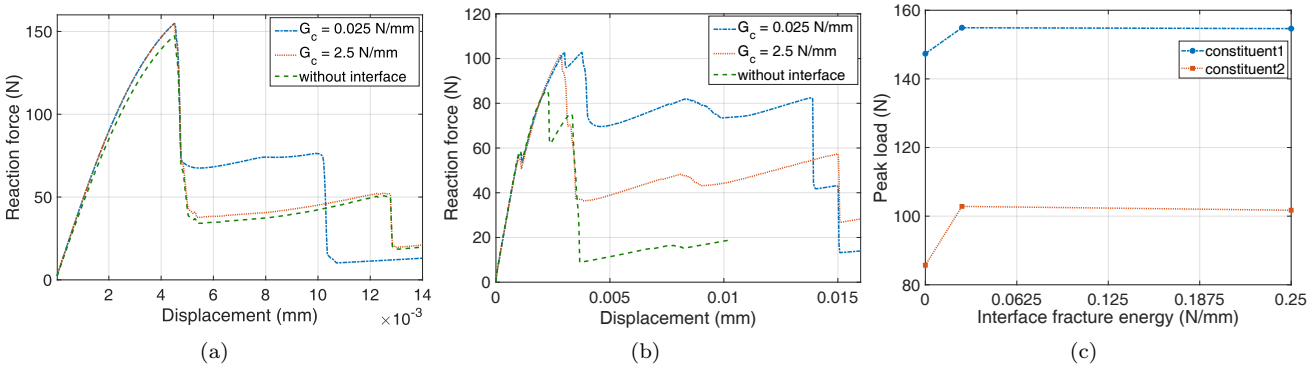

(a) (b) (c)

Figure 18: Comparison of traction vs. displacement plots considering the six layered composite shown in Fig. 15, when the layers are perfectly bonded and joined through interfaces fracture energy equal to 0.025 N/mm and 2.5 N/mm, as described in (a) case 5 and (b) case 6. The peak loads for the cases in (a) and (b) are plotted in (c). A perfectly bonded interface is identified by zero fracture energy of the interface.

3.4.2. Case 6: Crack in the constituent2 of multi-layer composite

The influence of layer sequence on crack propagation is studied by considering the crack in constituent2 as shown in Fig. 15(b), with and without the interface. Evolution of the phase field parameter with deformation is shown in Fig. 19. The top row Figs. 19(a-e) indicate the deformed configurations of the composite, whose layers are joined by an interface material of fracture energy equal 0.025 N/mm, corresponding to displacement loads of 0.00125 mm, 0.0029 mm, 0.00305 mm, 0.0095 mm and 0.01125 mm. Whereas, the bottom row Figs. 19(f-j) represent the deformed configurations of the perfectly joined composite without any interface material, and corresponding to displacement loads of 0.00125 mm, 0.002 mm, 0.0034 mm, 0.00435 mm and 0.00525 mm, respectively.

The influence of altering the layer sequence with interface is clear by comparing Figs. 16(a-e) and 19(a-e). Although the interface material is same in both cases, due to difference in stiffness the crack deflection is significant in this case. In case 5, the crack starts its propagation in a soft constituent1, which requires less fracture energy as compared to this case, where the crack initially starts its propagation in the stiff constituent2. As a result, the external load is shared by the constituent2 in this case, until reaching the interface, see Fig. 19(a). The interface helps in constituent1 elongation by distributing the load between constituent2 and constituent1 through shear transfer. Therefore, the crack is observed to traverse along the interface soon after arriving at the constituent2-constituent1 interface, see Fig. 19(b). Furthermore, the presence of multiple layers of soft constituent1 and the interfaces has resulted in generation of multiple inerfacial cracks as shown in Fig. 19(c). On the other hand, due to the continuous increase in external load the intermediate constituent2 layers were observed to fail in a brittle fashion leading to delamination and pull out from the constituent1, see Fig. 19(d). Finally the specimen separated into two parts when all the constituent2 were completely broken, see Fig. 19(e). Whereas, when the interfaces are perfectly bonded without any interface crack deflection across the interfaces is found to be totally absent, as shown in Figs. 19(f-j). Therefore, the crack is observed to simply transit from one layer to another during its propagation, as observed in case 4.

Variation of the reaction forces vs. displacement for case 6 is shown in Fig. 18(b), where the fracture toughness is found to be significantly higher in the presence interface. Furthermore, the influence of fracture energy of the interface on the overall toughness of the composite is evident by comparing the G_c curves. The toughness of multi-layered composite is observed to decrease with increase in fracture energy of the interface. A comparison of the peak loads in cases 5 and 6 is provided in Fig. 18(c), where the maximum load in case 5 is observed to be higher than that of case 6 for the given range of displacement. The total area of soft constituent1 in cases 5 and 6 is equal to 57.14% and 42.86%, respectively. Which infers that composite in case 5 absorbs higher energy as compared to the composite in case 6. Therefore, the fracture toughness of the composite with layer sequence in case 5 is higher as compared to case 6. However, the difference can be tuned for the requirement by adjusting the total number of layers and hence the area of constituent2 and material1s.

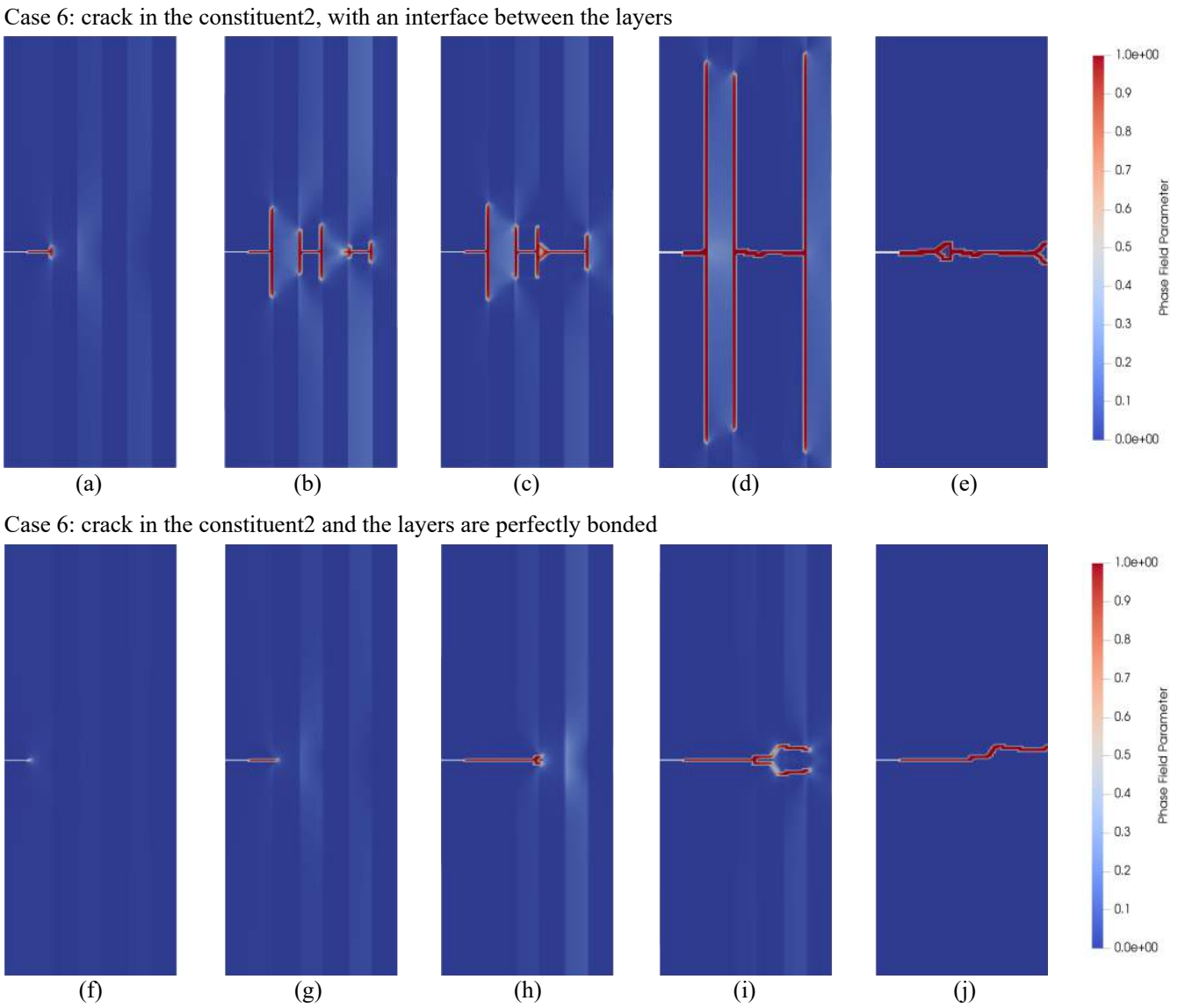

Figure 19: Crack in the constituent1: distribution of phase field parameter in the deformed configuration of multi-layer specimen made of six layers, as shown in Fig. 15(b). The top row indicates the configuration with an interface of fracture energy equal to 0.025 N/mm at applied displacements equal to (a) 0.00125 mm, (b) 0.0029 mm, (c) 0.00305 mm, (d) 0.0095 mm and (e) 0.01125 mm. The corresponding configurations assuming a perfect bonding between the layers at displacement load equal to (f) 0.00125 mm, (g) 0.002 mm, (h) 0.0034 mm, (i) 0.00435 mm and (j) 0.00525 mm are shown in the bottom row.

3.5. Numerical example 5: crack propagation in unidirectional composite laminate

In the previous examples, the influence of interface on crack propagation in different layered composites is studied and noticed that the crack complexity increases with increase in number of composite layers. Also, the fracture toughness of composite is observed to depend on the interface properties. Furthermore, crack is observed to deflect along the interface in the presence of interface, before penetrating into bulk.

In this example, a variety of composites with different constituent1 and constituent2 layups and spacing are considered to study the crack growth and hence the fracture toughness. Figure 20 shows the geometries and layup sequences of the composites along with their boundary conditions used in the analysis. Figures 20(a-c) and (d-f) denote the configurations when the crack is contained in the constituent1 and constituent2, respectively. In all cases, the domain is subjected to uni-axial tensile load such that the crack opens in mode I. An initial crack of size 0.25 mm located at mid height of the domain is considered in all cases. The length of the specimen is adopted as 6 mm, whereas, the total width (excluding interface thickness) is maintained as 1.5 mm. An interface of width equal to 0.005 mm is adopted to join the inter-layers. In order to study the influence of crack location on propagation two different scenarios are considered, crack in (i) constituent1 and (ii) constituent2, as shown in the top and bottom rows of Fig. 20, respectively. The width of layer1 is varied from 0.25 mm to 0.75 mm and the width of the remaining layers is adjusted such that the total width is maintained as 1.5 mm, see Fig. 20(a-f). The characteristic length l_0 is chosen as equal to $2h$, where h is the smallest element size in the domain.

The material parameters of constituent1 and constituent2 layers are shown in Table 2 and interface properties

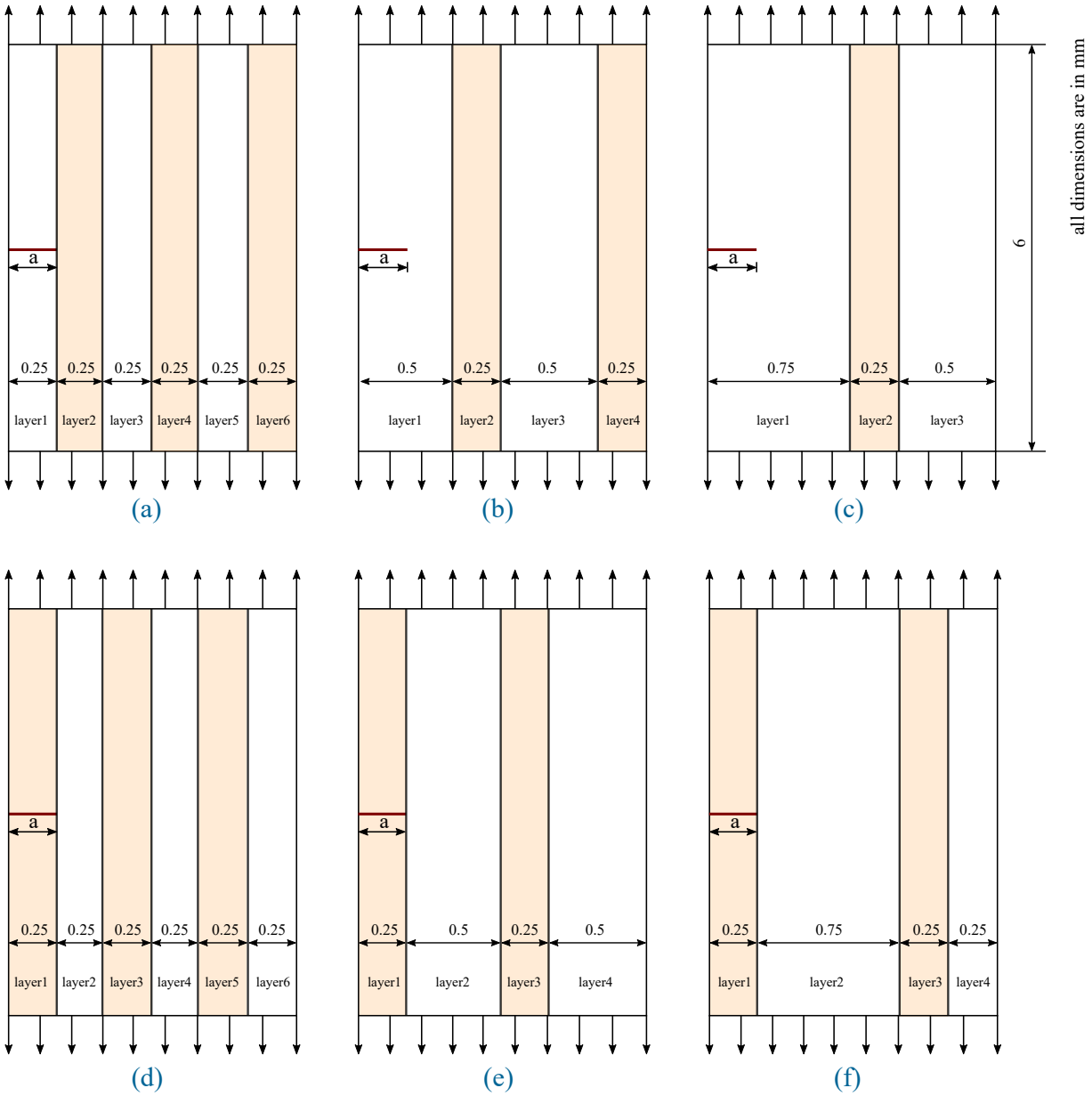

Figure 20: Schematic of single-edge notched composite specimen used in the simulations. Figures (a-c) and (d-f) denote the configurations when the crack is contained in the constituent1 and constituent2, respectively. The shaded region corresponds to constituent2.

are listed in Table 3. The domain in discretized with 4-noded QUAD-elements yielding a total of 15654 elements with 19977 nodes. Numerical simulations are performed considering a displacement load of 0.00001 mm per cycle until the fracture. Crack patterns considering an interface having fracture energy of 0.025 N/mm are compared to the crack patterns when the composite is made by completely bonded interfaces.

3.5.1. Case 7: crack in constituent1 layer of the composite

In this case, crack is contained in the constituent1 layer, and three difference scenarios with varying width of the constituent1 layer i.e., 0.25 mm, 0.5 mm and 0.75 mm are considered, followed by alternating constituent2 and constituent1 layers, as shown in Figs. 20(a-c). The objective is to identify the influence of layer width on crack growth. Furthermore, scenarios with and without interface in each of the above three layup sequences are also considered. Figure 21 indicate the deformed configurations of the composite when the layers are joined by an interface material of fracture energy equal 0.025 N/mm, at various applied displacement load steps as follows. The top row Figs. 21(a-e) are captured at displacements equal to 0.00195 mm, 0.00325 mm, 0.0046 mm, 0.014 mm and 0.0141 mm; whereas, the middle row Figs. 21(f-j) are captured at displacements loads equal to 0.0045 mm, 0.00485 mm, 0.01 mm, 0.01375 mm and 0.0142 mm and the bottom row Figs. 21(k-o) are captured at displacements equal to 0.00475 mm, 0.00525 mm, 0.0054 mm, 0.0175 mm and 0.0178 mm.

An observation of the deformed configurations in Fig. 21 indicate that the fracture toughness of the composite increases with increasing size of layer1, see Fig. 20(a-c). This is because with increase in size of the layer1, area

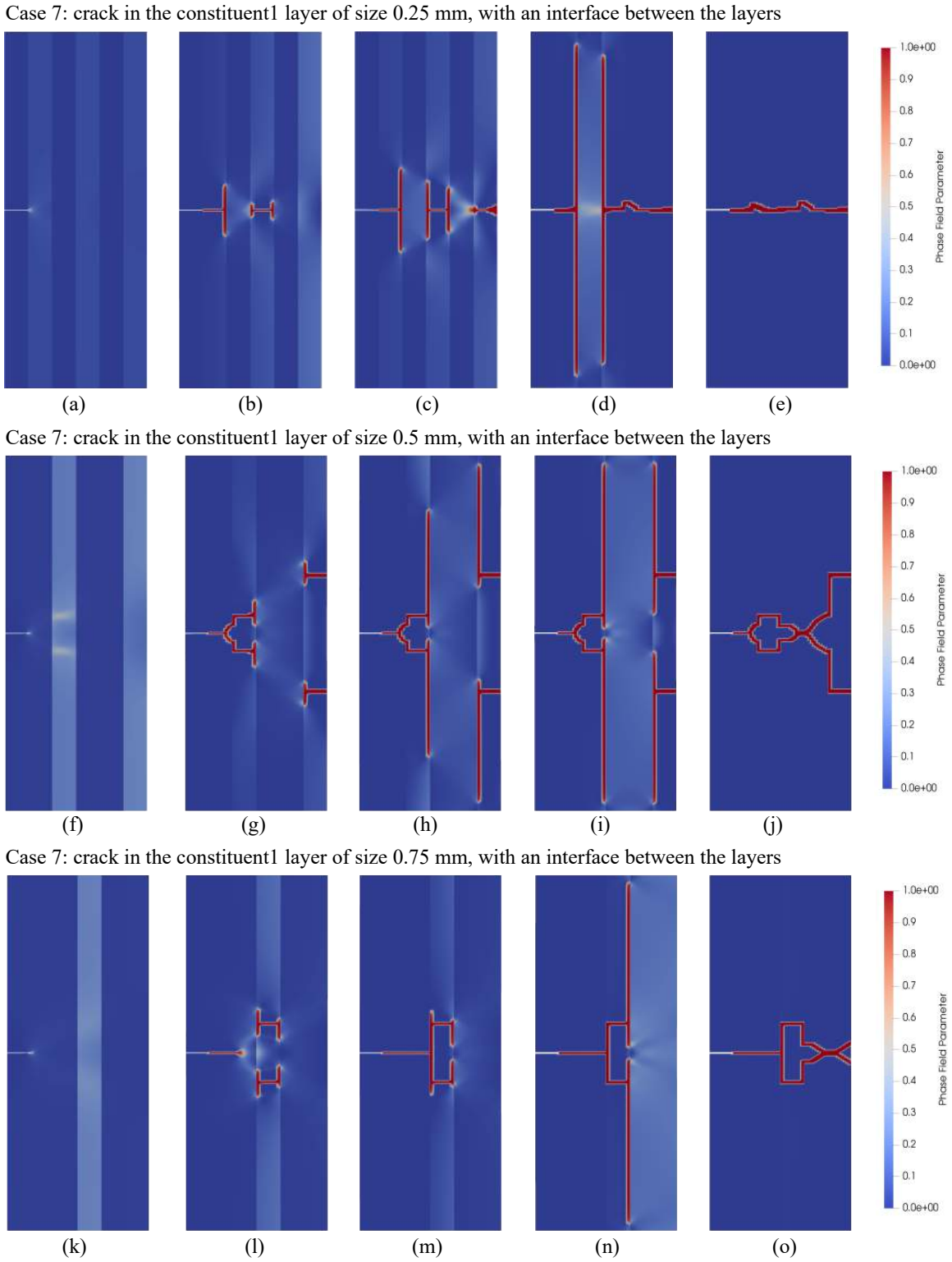

Figure 21: Crack in the constituent1: evolution of phase field parameter in the deformed configuration of composite specimens. Pictures in the top, middle and bottom rows indicate the deformed configurations of the specimens in Figs. 20(a), (b) and (c), respectively, considering an interface of fracture energy equal to 0.025 N/mm at various applied displacement load steps as follows. Top row: (a) 0.00195 mm, (b) 0.00325 mm, (c) 0.0046 mm, (d) 0.014 mm and (e) 0.0141 mm; middle row: (f) 0.0045 mm, (g) 0.00485 mm, (h) 0.01 mm, (i) 0.01375 mm and (j) 0.0142 mm and the bottom row: (k) 0.00475 mm, (l) 0.00525 mm, (m) 0.0054 mm, (n) 0.0175 mm and (o) 0.0178 mm.

of constituent1 also increases. For instance, the percentage areas of constituent1 in Figs. 20(a), (b) and (c) are indicate by 50, 66.67, and 83.34, respectively. This is reflected in displacement values at the time of fracture, which are observed to increase with increase in width of layer1. Whereas, Fig. 22 indicates the evolution of phase field parameter in the deformed configuration of composite specimens in Figs. 20(a), (b) and (c), respectively, considering perfectly joined interfaces at various applied displacement load steps as follows. The top row Figs. 22(a-e) are captured at displacements equal to 0.0025 mm, 0.00275 mm, 0.0035 mm, 0.0038 mm and 0.004

mm; the middle row Figs. 22(f-j) are captured at displacements loads equal to 0.0009 mm, 0.00094 mm, 0.001 mm, 0.00125 mm and 0.0055 mm and the bottom row Figs. 22(k-o) are captured at displacements loads equal to 0.000465 mm, 0.000515 mm, 0.00565 mm, 0.00605 mm and 0.0063 mm. According to Figs. 22(a-e), crack is observed to transit the inter layers until fracture. On the other hand, Figs. 22(f-j) and (k-o) indicates the crack initiation in the brittle constituent2 layers and propagation in large constituent1 layers. However, fracture toughness of the composite is found to be increasing with increasing width of layer1.

Variation of the reaction force with displacement for the cases in Figs. 20(a-c) are respectively shown in Figs. 23(a-c). The increase in constituent1 area is observed to increase the area under the under the curves in Figs. 23(a-c), in the presence of interface. The peak loads with increased width of layer1 containing the crack are listed in Table 4. Moreover, with increased percentage of constituent1 the increase in fracture energy of the interface does not have much improvement on the load carrying capacity of the composite. Based on the cases in this study, 66.67% of constituent1 is found yield the maximum fracture toughness of the composite, see Figs. 20(b) and 23(b).

	Peak load (N) when crack is contained in					
	constituent1 layer of width (mm)			**case shown in**		
Interface type ↓	**0.25**	**0.50**	**0.75**	Fig.20(d)	Fig.20(e)	Fig.20(f)
Perfectly bonded	110.04	130.77	112.44	96.81	75.67	75.51
Fracture energy (0.025 N/mm)	98.87	127.44	110.24	96.16	90.19	76.49
Fracture energy (2.5 N/mm)	100.48	127.62	110.92	109.90	159.25	152.39

Table 4: Peak loads for the cases shown in Figs. 20(a-f) are respectively shown in columns 2-7.

3.5.2. Case 8: crack in constituent2 layer of the composite

In this case, crack is contained in the constituent2 layer in three difference scenarios, see Figs. 20(d-f), with percentage of constituent1 areas of: 50, 66.67 and 66.67, respectively. The objective is to estimate the fracture toughness of the composite with percentage of constituent1. Furthermore, scenarios with and without interface in each of the above three layups are also considered. Figure 24 indicate the deformed configurations of the composite when the layers are joined by an interface material of fracture energy equal 0.025 N/mm, at various applied displacement load steps as follows. The top row Figs. 24(a-e) are captured at displacements equal to 0.0015 mm, 0.0031 mm, 0.00365 mm, 0.015 mm and 0.01515 mm; whereas, the middle row Figs. 24(f-j) are captured at displacements loads equal to 0.0015 mm, 0.003 mm, 0.00465 mm, 0.01525 mm and 0.01575 mm and the bottom row Figs. 24(k-o) are captured at displacements equal to 0.0015 mm, 0.004 mm, 0.0055 mm, 0.0135 mm and 0.01595 mm. Based on Fig. 23(d-f), the fracture toughness of the composite is observed to drastically increase with increase in constituent1 area. This is possible because of efficient load transfer across the interfaces.

Whereas, Fig. 25 indicates the evolution of phase field parameter in the deformed configuration of composite specimens in Figs. 20(d-f), considering perfectly interffaces at various applied displacement load steps as follows. The top row Figs. 25(a-e) are captured at displacements equal to 0.0015 mm, 0.00285 mm, 0.0033 mm, 0.0036 mm and 0.00375 mm; middle row Figs. 25(f-j) are captured at displacements loads equal to 0.0015 mm, 0.003 mm, 0.0032 mm, 0.00435 mm and 0.00475 mm and the bottom row Fig. 25(k-o) are captured at displacements loads equal to 0.0015 mm, 0.003 mm, 0.0036 mm, 0.00375 mm and 0.0042 mm. According to top row Figs. 25(a-e), crack is observed to transit the inter layers until fracture. On the other hand, Figs. 25(f-j) and (k-o) indicates that the crack initiation in the brittle constituent2 layers and propagation in large constituent1 layers. However, fracture toughness of the composite is found to be decreasing with increased constituent1 area.

When the initial crack size is equal to the size of constituent2 (see Figs. 20(d-f)), the situation can be considered as cracked constituent2. When such specimen is loaded in mode I, multiple breakage of constituent2 is observed as the crack propagates. The fracture toughness is significantly influenced by the interface connecting last two layers, which is backed by constituent1. In order to propagate into constituent1 large load is required. Therefore, crack is observed to significantly traverse along the interface before penetrating into the last constituent1 layer, see Fig. 24. On the other hand, in absence of interface, crack can easily penetrates into last constituent1 layer, see Fig. 25. Due to their low fracture toughness, constituent2 can easily break, producing several parallel cracks. Therefore, before the fracture of the composite, crack branching and penetration merge together as shown in Fig. 25.

Figures 23(d-f) represent the variation of the reaction force with displacement for the cases in Figs. 20(d-f). The corresponding peak loads are listed in columns 5 to 7 in Table 4. A comparison of the load displacement curves for the cases in Figs. 20(a) and (d), 20(b) and (e), and 20(c) and (f) are provided in Figs. 23(g), (h) and (i), respectively. Based on Figs. 23(g-i), fracture toughness of the composite when the crack is contained in constituent2 layer is higher compared to the cases when crack is contained in the constituent1. Furthermore, a comparison of the load-displacement plots considering an interface of fracture energy 0.025 N/mm for cases

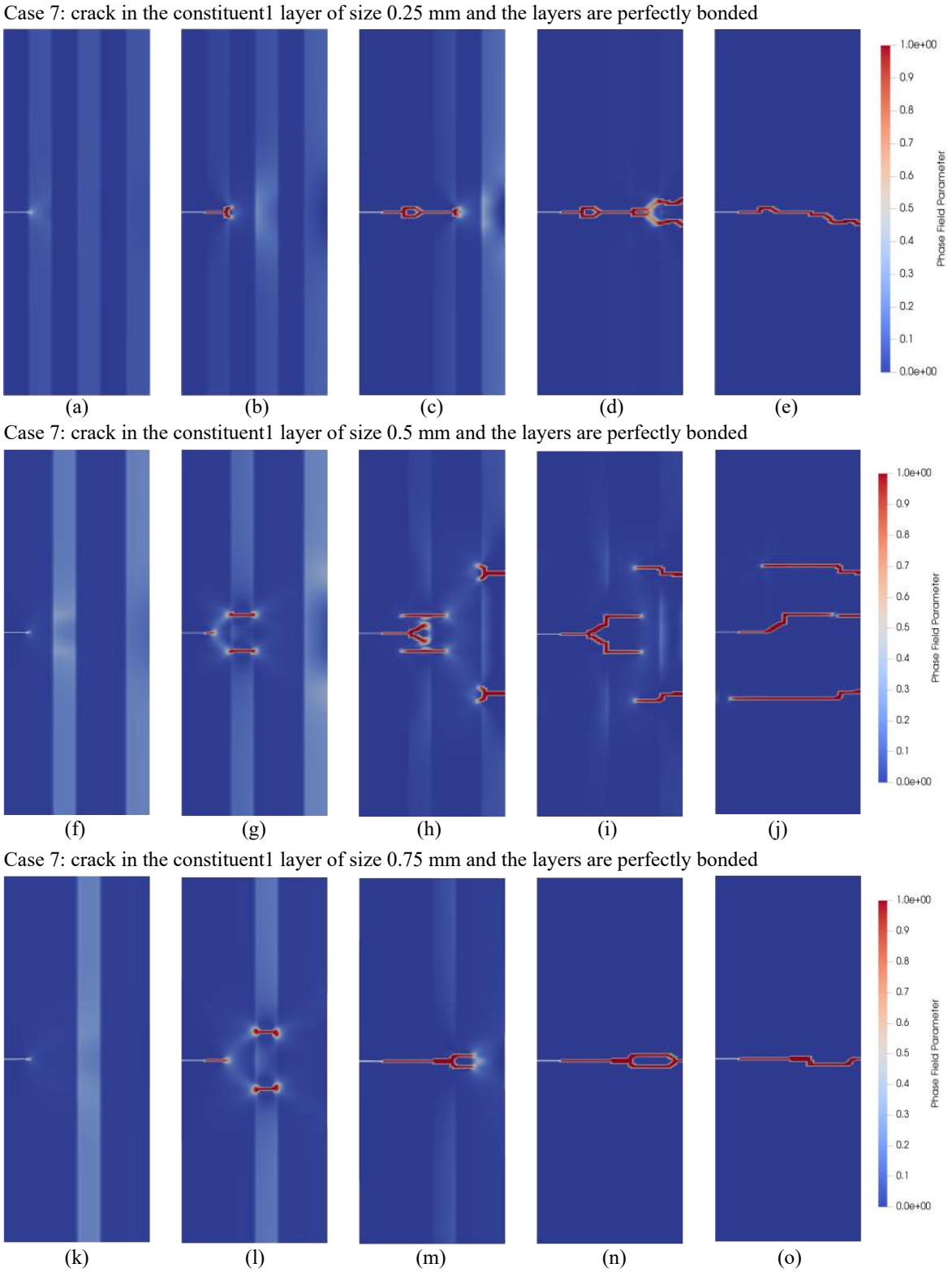

Figure 22: Crack in the constituent1: evolution of phase field parameter in the deformed configuration of composite specimens. Pictures in the top, middle and bottom rows indicate the deformed configurations of the specimens in Figs. 20(a), (b) and (c), respectively, considering perfectly bonded interfaces at various applied displacement load steps as follows. Top row: (a) 0.0025 mm, (b) 0.00275 mm, (c) 0.0035 mm, (d) 0.0038 mm and (e) 0.004 mm; middle row: (f) 0.0009 mm, (g) 0.00094 mm, (h) 0.001 mm, (i) 0.00125 mm and (j) 0.0055 mm and the bottom row: (k) 0.000465 mm, (l) 0.000515 mm, (m) 0.00565 mm, (n) 0.00605 mm and (o) 0.0063 mm.

in Figs. 20(a-c) and 20(d-f) are provided in Figs. 26(a) and (b), respectively, along with highlighting the peak loads. The area under the curves in Fig. 26(b) is certainly higher compared to the area under the curves in Fig. 26(a). Therefore, crack in constituent1 case is more dangerous compared to the constituent2 pull out.

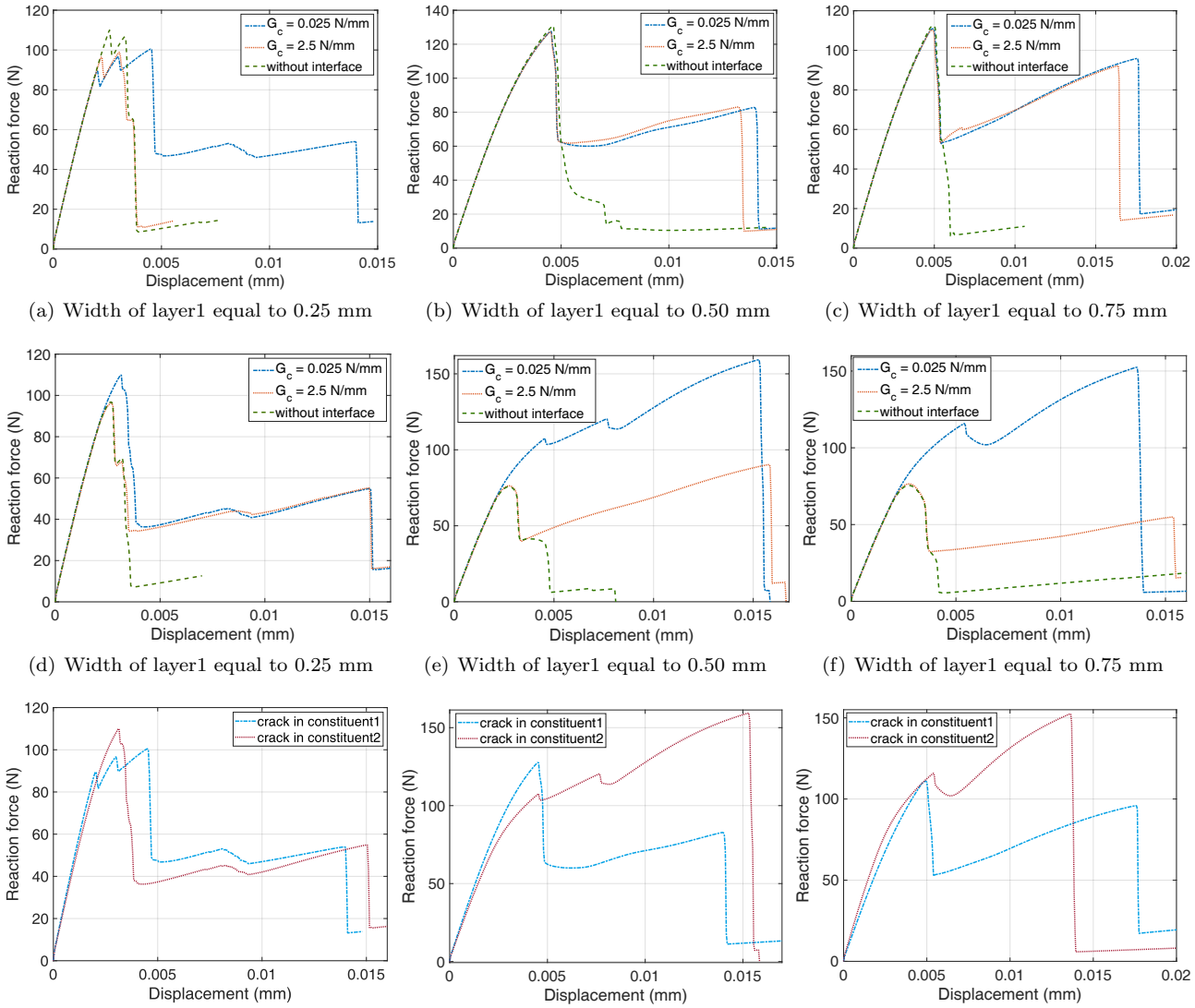

(a) Width of layer1 equal to 0.25 mm (b) Width of layer1 equal to 0.50 mm (c) Width of layer1 equal to 0.75 mm

(d) Width of layer1 equal to 0.25 mm (e) Width of layer1 equal to 0.50 mm (f) Width of layer1 equal to 0.75 mm

(g) Interface G_c equal to 0.025 N/mm (h) Interface G_c equal to 0.025 N/mm (i) Interface G_c equal to 0.025 N/mm

Figure 23: Crack in the constituent1: (a-c) Traction-displacement plot for composite specimens shown in Figs. 20(a-c), respectively. Crack in the constituent2: (d-f) Traction-displacement plot for composite specimens shown in Figs. 20(d-f), respectively. A comparison of the reaction force vs. displacement plots considering an interface of fracture energy 0.025 N/mm, when the crack is contained in constituent1 and constituent2 are shown in figures (g-i), where the corresponding cases are adopted from figures (a) and (d), figures (b) and (e), and figures (c) and (f), respectively.

3.6. Numerical example 6: crack propagation in composite laminate under transverse loading

In earlier cases, the influence of constituent2 spacing on crack propagation is studied considering unidirectional composite laminate loaded axially, where the failure is observed to be brittle. Furthermore, properties of the interface played prominent role on fracture toughness of the composite. In this example, influence of interface on crack propagation when unidirectional composite laminate is subjected to transverse loading is studied. A schematic showing the geometry and boundary conditions of the composite under transverse loading is shown in Fig. 27.

Crack propagation is studied in a single-edge notched composite lamina with l_y equal to 0.25 mm, and the layers are connected by an interface of fracture energy equal to 0.025 N/mm. The specimen is subjected to transverse mode I loading with a displacement load of 0.00001 mm per cycle until fracture. The deformed configurations highlighting the evolution of crack pattern are shown in Figs. 28(a-e), captured when the applied displacement is equal to 0.00375 mm, 0.004 mm, 0.00425 mm, 0.0044 mm and 0.0046 mm, respectively. The crack is observed to propagate through the constituent1 until fracture. The interface has no influence on the crack propagation.

3.7. Numerical example 7: crack propagation in woven composite laminate

In this example, crack propagation in woven composite laminate is studied considering an interface of fracture energy equal to 0.025 N/mm and also assuming that the layers are perfectly bonded. Figure 29 shows a

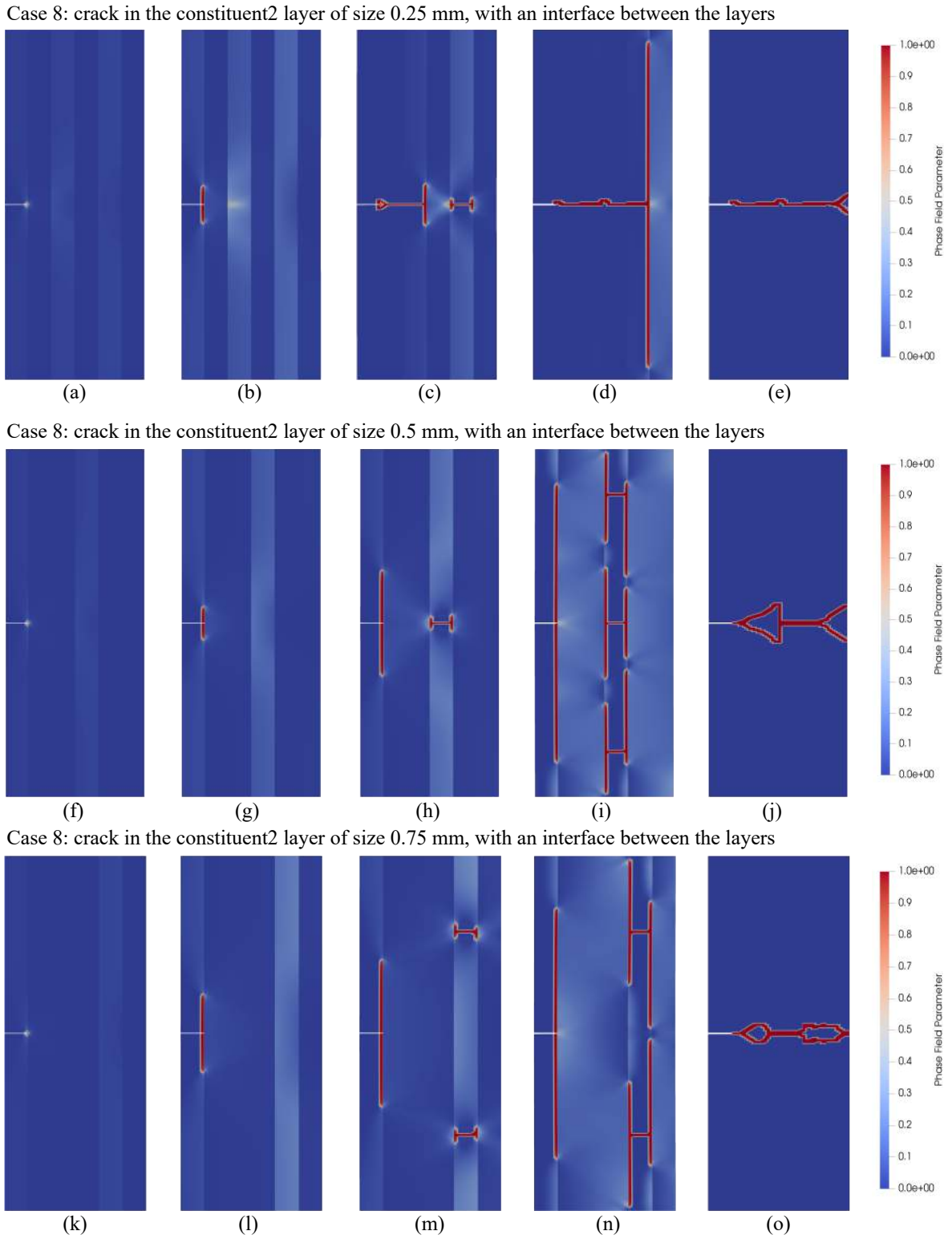

Figure 24: Crack in the constituent2: evolution of phase field parameter in the deformed configuration of composite specimens. Pictures in the top, middle and bottom rows indicate the deformed configurations of the specimens in Figs. 20(d), (e) and (f), respectively, considering an interface of fracture energy equal to 0.025 N/mm at various applied displacement load steps as follows. Top row: (a) 0.0015 mm, (b) 0.0031 mm, (c) 0.00365 mm, (d) 0.015 mm and (e) 0.01515 mm; middle row: (f) 0.0015 mm, (g) 0.003 mm, (h) 0.00465 mm, (i) 0.01525 mm and (j) 0.01575 mm and the bottom row: (k) 0.0015 mm, (l) 0.004 mm, (m) 0.0055 mm, (n) 0.0135 mm and (o) 0.01595 mm.

schematic of single edged notched woven composite laminate along with the boundary conditions used in the analysis. The domain is subjected to a uni-axial load. The specimen contains an initial edge notch of size 0.25 mm. Width of both constituent1 and constituent2 layers is considered as 0.25 mm. The overall length and width of the specimen are 6 mm and 1.5 mm, respectively.

Crack patterns in the woven composite lamina when the layers are connected by an interface of fracture energy equal to 0.025 N/mm are shown in the top row Figs. 30(a-e). The deformed configurations are captured

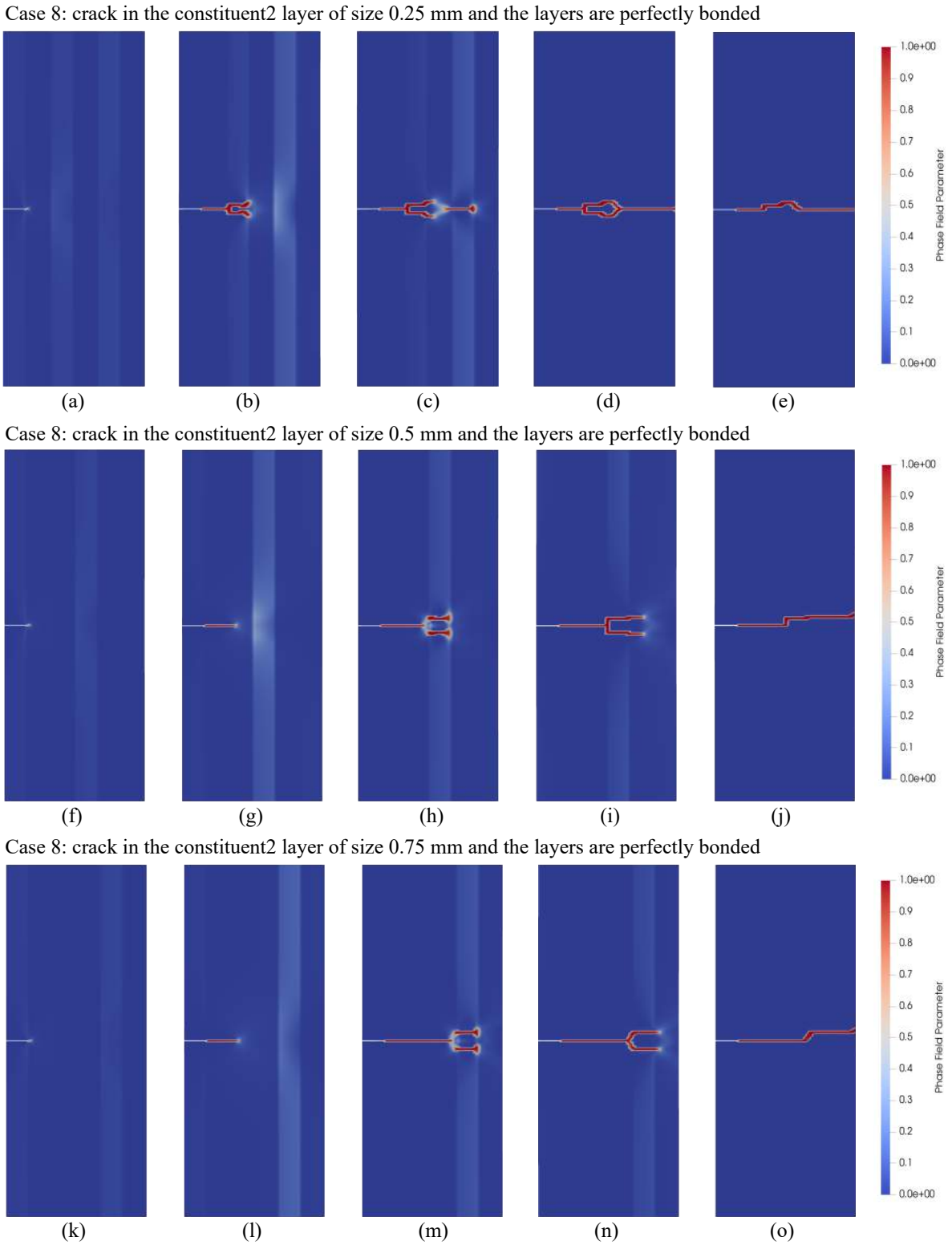

Figure 25: Crack in the constituent2: evolution of phase field parameter in the deformed configuration of composite specimens. Pictures in the top, middle and bottom rows indicate the deformed configurations of the specimens in Figs. 20(d), (e) and (f), respectively, considering perfectly bonded interfaces at various applied displacement load steps as follows. Top row: (a) 0.0015 mm, (b) 0.00285 mm, (c) 0.0033 mm, (d) 0.0036 mm and (e) 0.00375 mm; middle row: (f) 0.0015 mm, (g) 0.003 mm, (h) 0.0032 mm, (i) 0.00435 mm and (j) 0.00475 mm and the bottom row: (k) 0.0015 mm, (l) 0.003 mm, (m) 0.0036 mm, (n) 0.00375 mm and (o) 0.0042 mm.

when the applied displacement is equal to 0.00215 mm, 0.00295 mm, 0.00325 mm, 0.004 mm and 0.00425 mm. Based on Figs. 30(a-e), it is observed that when loaded in mode I, the initiated crack is deflected along interface up to constituent2. Upon further loading, crack deflects along the horizontal interface, as shown in Fig. 30(c). On the other hand, when the layers are perfectly bonded, crack branching happens due to failure of constituent2 followed by further propagation until fracture, see Figs. 30(f-j). Based on the load-displacement plot shown

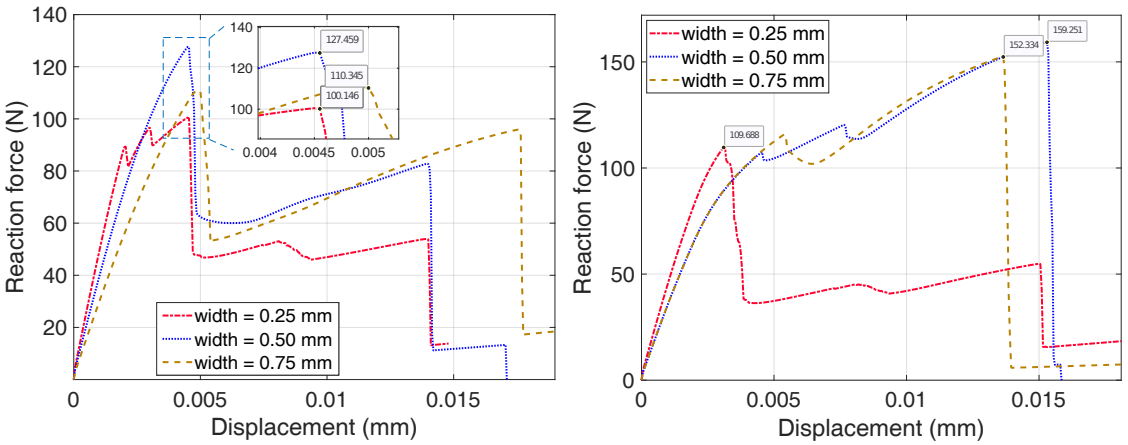

(a) Crack in the constituent1 (b) Crack in the constituent2

Figure 26: Comparison of load-displacement curves of composite laminates with interface of fracture energy equal to 0.025 N/mm, when the crack is contained in (a) constituent1, see Figs. 23(a-c) and (b) constituent2, see Figs. 23(d-f). Values of the peak loads are also highlighted.

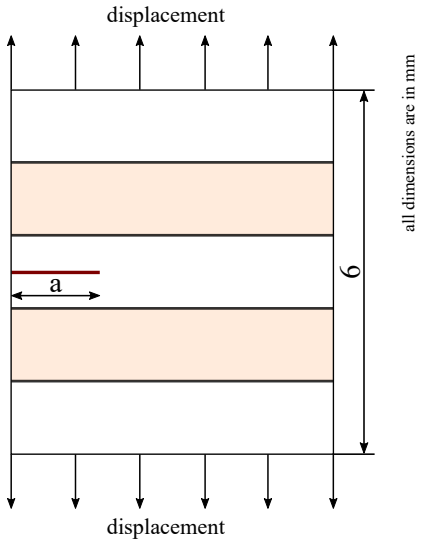

Figure 27: Schematic of a single edged notched uni-directional composite laminate subjected to transverse loading.

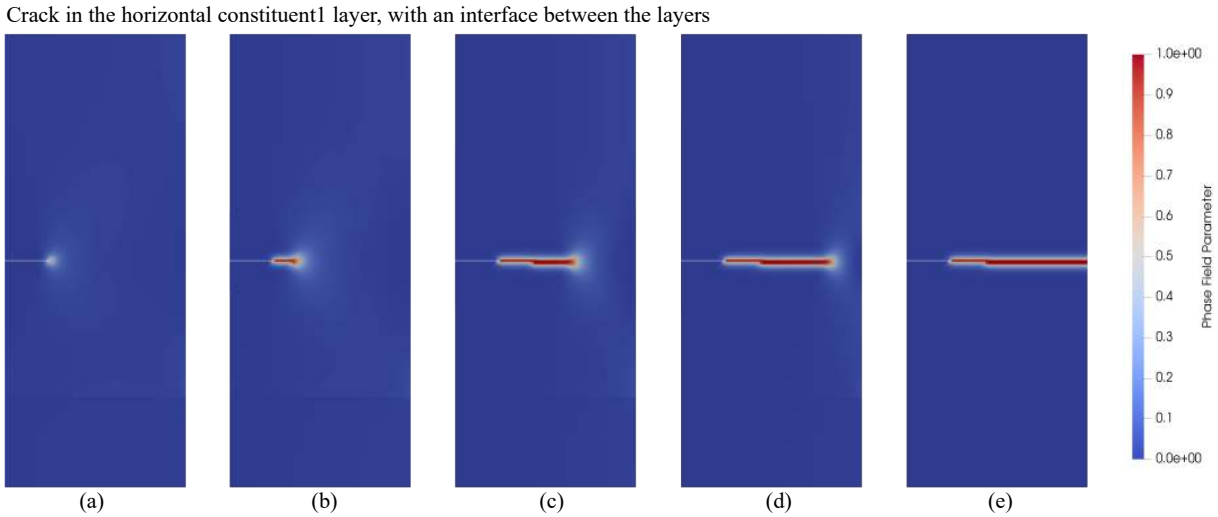

Figure 28: Crack propagation in a single-edge notched composite lamina with $l_y = 0.25$ mm, and the layers are connected by an interface of fracture energy equal to 0.025 N/mm, subjected to transverse mode I loading. The deformed configurations are captured when the applied displacement is equal to (a) 0.00375 mm, (b) 0.004 mm, (c) 0.00425 mm, (d) 0.0044 mm and (e) 0.0046 mm.

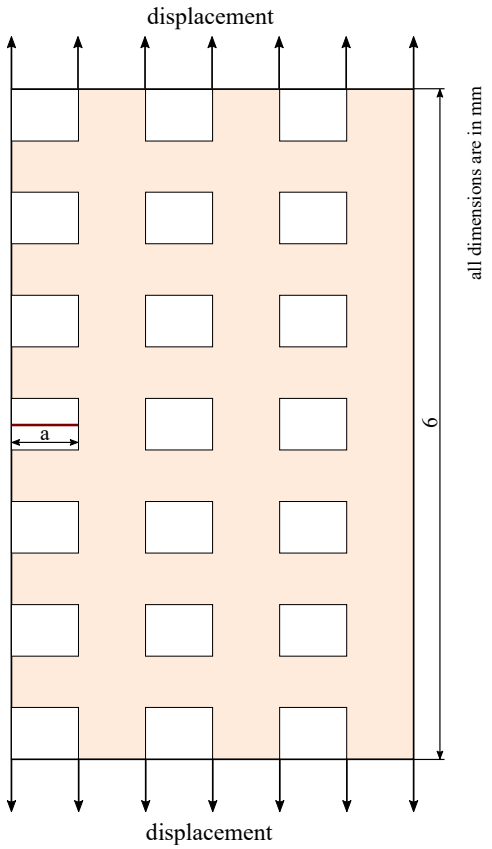

Figure 29: Schematic of single edged notched woven composite laminate

in Fig. 31, higher fracture toughness is observed for perfectly bonded layers. This is because, in the presence of interface crack propagates along horizontal interface, which reduces the overall fracture toughness of the composite laminate.

4. Conclusions

In this work, the investigation to study the crack propagation in composite laminates has been carried out. A numerical strategy by combining the phase field approach to simulate brittle fracture and the cohesive zone model to model the interface failure is herewith exploited. The study shows that introducing interface improves fracture toughness of the composite. Derived from the current study, it is observed that penetration vs deflection events depends on the properties of interface. When the initial crack is considered within the material with low fracture toughness, crack is observed to travel across the interface, realized by crack deflection along the interface.

The numerical study is carried out for bi-layer, tri-layered and multi-layer and woven composites considering critical fracture energies equal to 0.025 N/mm, 2.5 N/mm and no interface respectively. The crack is observed grow along the interfaces, followed by branching and separation into two parts. The comparative study shows that for cases like bi-layered and tri-layered laminates with interfaces evidences improved fracture toughness. While in case of multi-layered laminates it depends on interface properties along with crack complexity generated during loading.

The influence of the width of the constituent1 in crack propagation is also studied by varying its width from 0.25 mm to 0.75 mm. The fracture toughness is observed to increase with increase in the area of constituent1. Furthermore, under the unidirectional loading constituent2 is found to absorb more load. However, due to its low fracture toughness constituent2 fails first, leading to interfacial crack growth followed by crack branching. Depending on the critical fracture energy ratios crack further deflects or penetrates into the bulk. The crack propagation considering the initial crack in constituent2 is also studied. In all the cases, the fracture toughness is observed to be improved in the presence of interface.

Study on woven composites indicates that depending on the type of interface, the fracture toughness increases or reduces. For instance, when the interface with fracture toughness equal to 0.025 N/mm is considered, crack is observed to travel up to the interface, followed by further propagation along the horizontal laminae, which lowers the fracture toughness when compared to perfectly bonded interfaces.

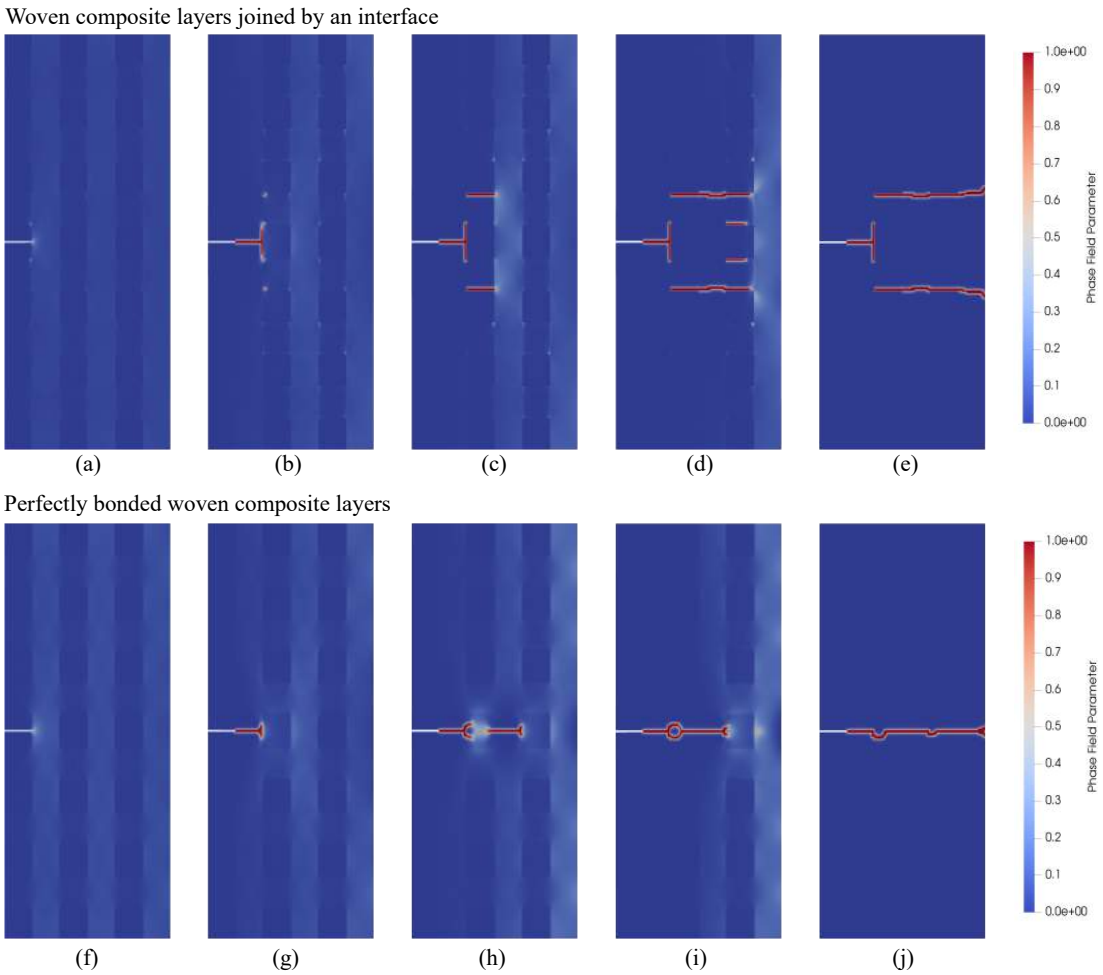

Figure 30: Crack propagation in a single-edge notched woven composite lamina. Top row figures indicate the deformed configurations when the layers are connected by an interface of fracture energy equal to 0.025 N/mm at applied displacement is equal to (a) 0.00215 mm, (b) 0.00295 mm, (c) 0.00325 mm, (d) 0.004 mm and (e) 0.00425 mm. The corresponding configurations assuming a perfect bonding between the layers at displacements load equal to (f) 0.000275 mm, (g) 0.0003 mm, (h) 0.0043 mm, (i) 0.00455 mm and (j) 0.0048 mm.

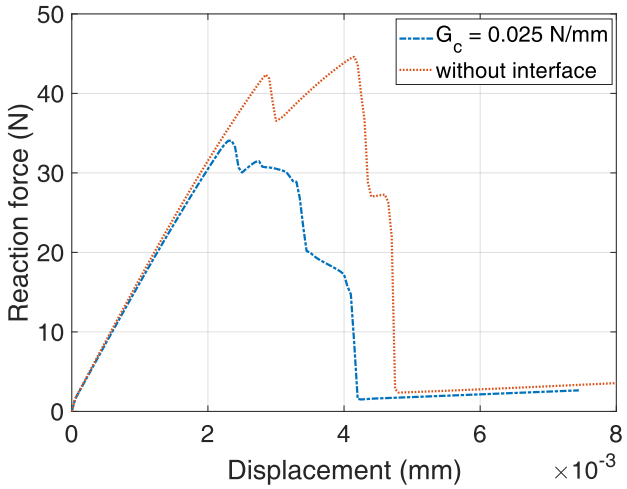

Figure 31: Comparison of traction vs displacement plots of the woven composite with an interface fracture energy energy equal to 0.025 N/mm, and perfectly bonded layers.

Acknowledgements

Budarapu thankfully acknowledges the financial support from IIT Bhubaneswar through the seed project SP-097, titled "Multiphysics Analysis of Cracked Photovoltaic Solar cells". Support from the Italian Ministry of Education, University and Research to the Project of Relevant National Interest 2017 (PRIN) "XFAST-SIMS: Extra fast and accurate simulation of complex structural systems" is gratefully acknowledged by Paggi.

Reinoso is grateful to the Consejería de Economóa y Conocimiento, Junta de Andalucía, and Ministerio de Ciencia, Innovación y Universidades, through project PID2019-109723GB-I00.

References

[1] YBS Sudhir, PR Budarapu, N Madhavi, and Y. Krishna. Buckling analysis of thin wall stiffened composite panels. *Computational Materials Science*, 96B:459–471, 2015. doi:10.1016/j.commatsci.2014.06.007.

[2] YBS Sudhir, PR Budarapu, Y Krishna, and S. Devraj. Studies on ballistic impact of the composite panels. *Theoretical and Applied Fracture Mechanics*, 72:2–12, 2014. doi:10.1016/j.tafmec.2014.07.010.

[3] H Shetty, D Sethuram, B Rammohan, and PR Budarapu. Low-velocity impact studies on gfrp and hybrid composite structures. *International Journal of Advances in Engineering Sciences and Applied Mathematics*, 12(3):125–141, 2020.

[4] PR Budarapu, B Rammohan, SK Vijay, BD Satish, and R. Raghunathan. Aero-elastic analysis of stiffened composite wing structure. *Journal of Vibration Engineering & Technologies*, 8(3):255–264, 2009.

[5] Y Kumar, B Rammohan, PR Budarapu, DK Harursampath, and KN Seetharamu. Dynamic instability analysis of multifunctional composite structures. *AIAA Journal*, pages 1–14, 2019.

[6] IG García, M Paggi, and V Mantič. Fiber-size effects on the onset of fiber–matrix debonding under transverse tension: a comparison between cohesive zone and finite fracture mechanics models. *Engineering Fracture Mechanics*, 115:96–110, 2014.

[7] BL Wang, YG Sun, and HY Zhang. Multiple cracking of fiber/matrix composites-analysis of normal extension. *International Journal of Solids and Structures*, 45(14-15):4032–4048, 2008.

[8] PR Budarapu, S Thakur, S Kumar, and M Paggi. Micromechanics of engineered interphases in nacre-like composite structures. *Mechanics of Advanced Materials and Structures*, pages 1–16, 2020.

[9] SL Phoenix and IJ Beyerlein. *Comprehensive Composites*, volume 1, chapter Statistical strength theory for fibrous composite materials, pages 559–639. Elsevier: Amsterdam, 2000.

[10] J Inoue, S Nambu, Y Ishimoto, and T Koseki. Fracture elongation of brittle/ductile multilayered steel composites with a strong interface. *Scripta Materialia*, 59(10):1055–1058, 2008.

[11] F Rebillat, J Lamon, and A Guette. The concept of a strong interface applied to sic/sic composites with a bn interphase. *Acta materialia*, 48(18-19):4609–4618, 2000.

[12] H Liu and SM Hsu. Fracture behavior of multilayer silicon nitride/boron nitride ceramics. *Journal of the American Ceramic Society*, 79(9):2452–2457, 1996.

[13] J Cook and JE Gordon. A mechanism for the control of crack propagation in all-brittle systems. *Proceedings of the Royal Society of London. Series A. Mathematical and Physical Sciences*, 282(1391):508–520, 1964.

[14] PR Budarapu, S Kumar, B Gangadhara Prusty, and M Paggi. Stress transfer through the interphase in curved-fiber pullout tests of nanocomposites. *Composites Part B: Engineering*, 165:417–434, 2019.

[15] S Bueno and C Baudin. Design and processing of a ceramic laminate with high toughness and strong interfaces. *Composites Part A: Applied Science and Manufacturing*, 40(2):137–143, 2009.

[16] V Tvergaard. Effect of fibre debonding in a whisker-reinforced metal. *Materials science and engineering: A*, 125(2):203–213, 1990.

[17] AR Zak and ML Williams. Crack point stress singularities at a bi-material interface. *Journal of Applied Mechanics*, 30:142–143, 1963.

[18] He MY and Hutchinso JWn. Crack deflection at an interface between dissimilar elastic materials. *International Journal of Solids and Structures*, 25:1053–1067, 1989.

[19] JP Parmigiani and MD Thouless. The roles of toughness and cohesive strength on crack deflection at interfaces. *Journal of the Mechanics and Physics of Solids*, 54(2):266–287, 2006.

[20] G Francfort and J-J Marigo. Revisiting brittle fracture as an energy minimization problem. *Journal of the Mechanics and Physics of Solids*, 46(8):1319–1342, 1998.

[21] C Miehe, F Welschinger, and M Hofacker. Thermodynamically consistent phase-field models of fracture: Variational principles and multi-field fe implementations. *International journal for numerical methods in engineering*, 83(10):1273–1311, 2010.

[22] A Raina and C Miehe. A phase-field model for fracture in biological tissues. *Biomechanics and modeling in mechanobiology*, 15(3):479–496, 2016.

[23] C Kuhn and R Müller. Phase field simulation of thermomechanical fracture. In *PAMM: Proceedings in Applied Mathematics and Mechanics*, volume 9, pages 191–192. Wiley Online Library, 2009.

[24] MA Msekh, JM Sargado, M Jamshidian, PM Areias, and T Rabczuk. Abaqus implementation of phase-field model for brittle fracture. *Computational Materials Science*, 96:472–484, 2015.

[25] V Carollo, J Reinoso, and M Paggi. Modeling complex crack paths in ceramic laminates: A novel variational framework combining the phase field method of fracture and the cohesive zone model. *Journal of the European Ceramic Society*, 38(8):2994–3003, 2018.

[26] M Paggi and J Reinoso. Revisiting the problem of a crack impinging on an interface: a modeling framework for the interaction between the phase field approach for brittle fracture and the interface cohesive zone model. *Computer Methods in Applied Mechanics and Engineering*, 321:145–172, 2017.

[27] V Carollo, J Reinoso, and M Paggi. A 3d finite strain model for intralayer and interlayer crack simulation coupling the phase field approach and cohesive zone model. *Composite Structures*, 182:636–651, 2017.

[28] J Reinoso, P Durand, PR Budarapu, and M Paggi. Crack patterns in heterogenous rocks using a combined phase field-cohesive interface modeling approach: A numerical study. *Energies*, 12(6):965, 2019.

[29] Hirshikesh, S Natarajan, and RK Annabattula. Modeling crack propagation in variable stiffness composite laminates using the phase field method. *Composite Structures*, 209:424–433, 2019.

[30] D Pranavi, A Rajagopal, and JN Reddy. Interaction of anisotropic crack phase field with interface cohesive zone model for fiber reinforced composites. *Composite Structures*, 270:114038, 2021.

[31] C Miehe, Hofacker M, and Welschinger F. A phase field model for rate-independent crack propagation: Robust algorithmic implementation based on operator splits. *Computer Methods in Applied Mechanics and Engineering*, 199(45-48):2765–2778, 2010.

[32] CV Verhoosel and R de Borst. A phase-field model for cohesive fracture. *International Journal for numerical methods in Engineering*, 96(1):43–62, 2013.

[33] B Bourdin, GA Francfort, and Jean-Jacques Marigo. The variational approach to fracture. *Journal of elasticity*, 91(1):5–148, 2008.
[34] JG Williams and H Hadavinia. Analytical solutions for cohesive zone models. *Journal of the Mechanics and Physics of Solids*, 50(4):809–825, 2002.